The Design and Characterization of a High-Resolution Imaging System

by

Kahan M^{c}Affer Dare

A THESIS SUBMITTED IN PARTIAL FULFILLMENT OF
THE REQUIREMENTS FOR THE DEGREE OF

BACHELOR OF SCIENCE

in

The Faculty of Science

(Physics)

THE UNIVERSITY OF BRITISH COLUMBIA

(Vancouver)

April 2014

Abstract

The aim of this thesis is to design and characterize an imagining system capable of resolution on a few micron scale. This system was characterized based off of how it transformed the image of a 1μm pinhole. It was found that the system performed better if the the aperture was placed between the aspheric and the dichroic mirror as opposed to placing it before the aspheric. The full system was found to have a resolution of at least 2μm based off of the FWHM of the diffraction pattern from the pinhole. A strong asymmetry was found when the full system was assembled and it was further enhanced when the aperture was displaced from the Fourier plane. While the cause was not determined, most of the elements were eliminated as the origin of the asymmetry. The experimental procedure for investigating the momentum space entanglement of a degenerate fermi gas was subsequently detailed along with the plans for creating a novel new device called a dilating lattice.

Table of Contents

Appendices

List of Tables

List of Figures

Acknowledgements

First, I would like to thank my phenomenal supervisor Kirk Madison for opening my eyes to the world of AMO. His endless enthusiasm has helped me not only write this thesis, but also to create a unique academic path for me to follow. I look forward to continuing our work over the coming years.

This wouldn't have been possible without the guidance and patience from all of the graduate students in our lab. Will, Mariusz and William have been great at explaining things and putting up with my constant flow of questions. I probably would have taken twice as long if Janelle hadn't been able to show me around the lab on a regular basis and keep me safe (I would be blind if you hadn't showed me how bright the 780nm light actually was). Lastly, Gene has taught me so many things, from aligning to properly estimating how long lab tasks actually take.

Chapter 1

Introduction and Motivation

In recent years, due to a series of breakthroughs, the area of Atomic, Molecular and Optical Physics (AMO) has progressed at an incredible rate. To augment regular cooling technology, physicists began using lasers, in conjunction with electric and magnetic fields, to manipulate particles. This method used radiation pressure to simultaneously localize and cool via the Zeeman and Doppler shifts respectively. These studies resulted in optical tweezers, lattices, dipole traps and magneto-optical traps. With these tools physicists were able to then experimentally create the first Bose-Einstein condensate (BEC) in 1995 [3]. A BEC is a useful tool for studying a wide range of experimental topics from quark gluon plasmas (via a transient BEC), superfluid behaviour (via the BEC-BCS crossover), and black holes (via the flow of phonons in a BEC forming a sonic black hole).

One of the main methods of gathering data about an ultra-cold system is through either absorption or fluorescence imaging. Therefore, it is also important to develop imaging techniques to collect appropriately accurate data in such unique systems. Many imaging apparatus could either image very small microscopic systems with great precision, or image macroscopic systems, but not both. Hence, physicists set out to make imaging systems with higher resolution which would be able to probe both local and global properties of their systems. It wasn't until almost 15 years later that Markus Greiner [5] would develop the first so-called quantum gas microscope. Unfortunately, this system is technically difficult, expensive and required the subject of interest to be confined to a 2D plane.

However, this lead to many other groups developing their own high-resolution imaging systems, and this thesis details development of such an apparatus. This upgrade in imaging capability would result in a variety of new experimental opportunities. One of particular note is the ability to study many-body states through quantum noise analysis as proposed by Eugene Demler [4]. Such data might be taken through a so-called time-of-flight experiment, whereby a system is released from its trapping potential, allowed to expand and then subsequently imaged. One can then correlate the position of a particle with its momentum and hence study the underlying entanglement between modes in momentum-space.

With the recent interest in quantum information, such studies of entanglement have played a large role in developing areas from quantum cryptography to quantum gravity. As one of the many systems in which one can study entanglement, ultra-cold gases have the unique characteristic of having a very low noise level and a wealth of techniques to both manipulate and analyze systems.

Hence, developing an appropriate data acquisition apparatus is paramount, especially when it can have an impact on so many areas.

A more immediate, scientific motivation, for this imaging system is an experimental test of some recent work by Mark van Raamsdonk [1, 2]. These works consider the momentum-space entanglement in a fermi gas at ultra-cold temperatures and would therefore provide an interesting opportunity to compare theoretical and experimental results. It would expand on some previous work by Deborah Jin [6], which means it is a natural extension of the characterization tests for our imaging system. This is due to the fact that Jin's work provides a more simplistic case in which one can study momentum-space correlations which would serve as a benchmark test of the imaging apparatus. Arguably more important though, is the fact that experimentally checking van Raamsdonk's results presents a rare opportunity to test calculations done in the highly theoretic oriented realm of high-energy physics.

This system has been engineered to have a very high resolution, with the aim of doing these momentum-correlation measurements in order to compare with theoretical work. We present the design and characterization for the imaging system, as well as the necessary framework for the completion of the system in time.

1.1 High-Field Imaging

Another benefit to imaging along the vertical axis is the ability to image efficiently at high magnetic fields. By this, we mean that one of the transitions of interest requires circularly polarized imaging light in order for the light to interact with the particles. This imaging transition is from a state with $m_J = -1/2$ to $m_J = -3/2$ and our light will then need $\Delta m_J = -1$. This stems from the selection rules for this particular transition but what it means is that if the polarization is different, the light won't interact with the particles in the trap and therefore the image won't register any information regarding the particles.

In order for the particles to see purely right- or left-handed circularly polarized light, the light must propagate along the quantization axis of the atoms. It is at this point that the orientation of our system is important. As the magnetic field, generated by our coils, defines the axis of quantization to be along the vertical axis, as depicted in Figure 1.1. Hence, an imaging system aligned along the vertical axis is required in order to have the imaging light efficiently interact with the gas cloud.

Figure 1.1: A cartoon to demonstrate the basic environment which surrounds the ultra-cold gas. The arrows represent laser beams the create that Magneto Optical Trap (MOT) along with the current flowing in the rings which generates a magnetic field. In this arrangement, the particles in the MOT feel a spatially varying radiation pressure which localizes the cloud in the centre of the trap.

At present, the system is aligned horizontally which means that when the imaging light is projected onto the quantization axis, the best one can achieve is an even superposition of right- and left-handed circularly polarized light. This is produced by having light linearly polarized, with a changing projection onto the horizontal axis which results in the highest scattering rate for this orientation. Unfortunately, this means that each atom only interacts with every second photon. This causes a severe undercounting of the number of particles in the trap because much more light passes through the cloud than one might expect. This means the imaging system would then be much more susceptible to noise since the intensity of the signal is halved. This can be corrected during the analysis, but that in itself has complications. Therefore, having the imaging system aligned along the quantization axis would be beneficial for high-field imaging.

Chapter 2

Imaging Theory

Considering the bulk of this thesis is centred on building an imaging apparatus, it seems appropriate to first discuss the relevant background theory. We will start by comparing our system with an analogous camera which a photographer might use. These cameras usually consist of a main lens, an aperture and film. Different lenses are used to give different magnification and focal length, while different sensors change the resolution and noise. Lastly, the role of the aperture is to adjust how much light reaches the sensor. When someone wishes to adjust their images further, they can buy filters that block out light of certain wavelengths, or polarizers that only allow light of a certain polarization to pass through.

Each of these elements is present in the design of our imaging system and they each play a critical role in its setup. The two main elements on which we will focus, however, are the lens and the aperture, as the rest play more customary roles in the system. Hence, we will dedicate this section to their respective roles and how they can be used together to improve the quality of our system.

2.1 Fourier Optics

Before we discuss the specifics of our imaging theory, it will prove useful to review some of the concepts of Fourier optics. In doing so, we will develop the language in which we will discuss diffraction limited imaging and spatial filtering in the next couple of sections. At its core, Fourier optics is a description of the propagation of light in terms of individual waves of defined frequency. Thus it is heavily based on harmonic analysis and is most useful when applied to linear systems.

To start, we define the input of our system as some arbitrary function $f(x,y)$. This function has a corresponding Fourier transform $F(\nu_x,\nu_y)$ where ν_x and ν_y are the spatial frequencies in the x and y directions. They are called spatial frequencies because they are in units of cycles per unit length. Now, to give some meaning to $f(x,y)$, let us define a plane wave as

$$U(x,y,z) = Ae^{-i(k_x x + k_y y + k_z z)} \tag{2.1}$$

where A is some complex amplitude and $\vec{k}$ is the usual wavevector. We will henceforth write

$$f(x,y) = U(x,y,0) = Ae^{-2\pi i(\nu_x x + \nu_y y)} \tag{2.2}$$

where we have just used $2\pi\vec{\nu} = \vec{k}$. Note that $k^2 = (2\pi/\lambda)^2$ so one can determine $U(x,y,z)$ based off of $f(x,y)$. Since we can write an arbitrary travelling wave $U(x,y,z)$ as a superposition of these plane waves, if we understand how our imaging system transforms plane waves, we can then reconstruct how it transforms an arbitrary wave.

It is with this in mind that we define the transfer function $H(\nu_x,\nu_y)$ as the factor by which we multiply the initial harmonic function to get the output harmonic function. To illustrate, consider the initial harmonic function given in Equation 2.2 and how it would evolve travelling through space along the z-direction to some point d. Then we expect the output harmonic function to be given by

$$g(x,y) = Ae^{-2\pi i(\nu_x x+\nu_y y+\nu_z d)}. \tag{2.3}$$

Hence, we define the transfer function for free space, by a distance d, to be

$$H(\nu_x,\nu_y) = e^{-2\pi i d\sqrt{\lambda^{-2}-\nu_x^2-\nu_y^2}}. \tag{2.4}$$

In general, we write the output harmonic function as

$$g(x,y) = \int_{-\infty}^{\infty}\int_{-\infty}^{\infty} H(\nu_x,\nu_y)F(\nu_x,\nu_y)e^{-2\pi i(\nu_x x+\nu_y y)}d\nu_x d\nu_y \tag{2.5}$$

for some arbitrary transfer function.

Arguably more useful, and more directly applicable to many scenarios is the impulse response function $h(x,y)$ which characterizes how the system transforms a point source at the origin of the coordinate system. While it may not be immediately apparent, it is actually the Fourier transform of the transfer function $H(\nu_x,\nu_y)$. Hence, if we have two elements with transfer functions H_1 and H_2, we can multiply them or we can take the convolution of their respective impulse response functions. Thus, we get our general relation

$$g(x,y) = \int_{-\infty}^{\infty}\int_{-\infty}^{\infty} f(x',y')h(x-x',y-y')dx'dy' \tag{2.6}$$

relating the input and output waves via an arbitrary impulse response function.

2.1.1 Fourier Transform Via a Lens

A powerful tool in optics is the ability to take the Fourier transform of an image by placing a lens at a special point. Recall that a plane-wave, with a small incident angle θ_x, passing through a lens is transformed into a paraboloidal wave that is focused at some point $x = \theta_x f = \lambda\nu_x f$ as in Figure 2.1.

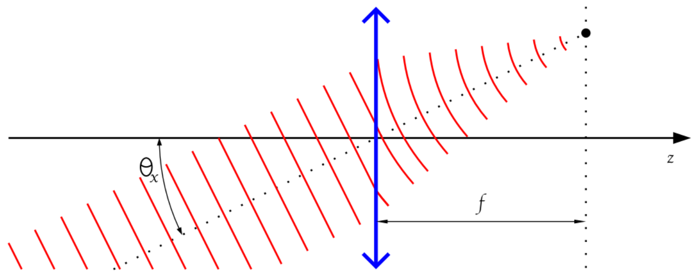

Figure 2.1: A plane wave, incident at an angle of θ_x is transformed, by a lens, into a paraboloidal wave focused at $x = \theta_x f$ where f is the focal length of the lens. This relationship is only valid for small angles θ_x.

Hence, we have that

$$g(x,y) \propto F\left(\frac{x}{\lambda f}, \frac{y}{\lambda f}\right) \tag{2.7}$$

At this point, we will skip the derivation of the proportionality factor as Equation 2.7 is all we will need to understand spatial filtering.

2.1.2 Spatial Filtering

Because lenses have this useful property that we can use them to take the Fourier transform of a signal, we can add other elements to manipulate this Fourier transform before reconstructing the image. The application we are concerned with is what's called spatial filtering. Just as the name implies, you place some sort of object or obstruction at the focal plane (also referred to as the Fourier plane) which subsequently blocks some of the frequencies from travelling further.

Most frequently this object will come in the form of an aperture, and it will then allow the lower frequencies to propagate while blocking the higher frequencies. It is interesting to note that although there are obstructions in the light's path, it can still retain most of the information as shown in Figure 2.2.

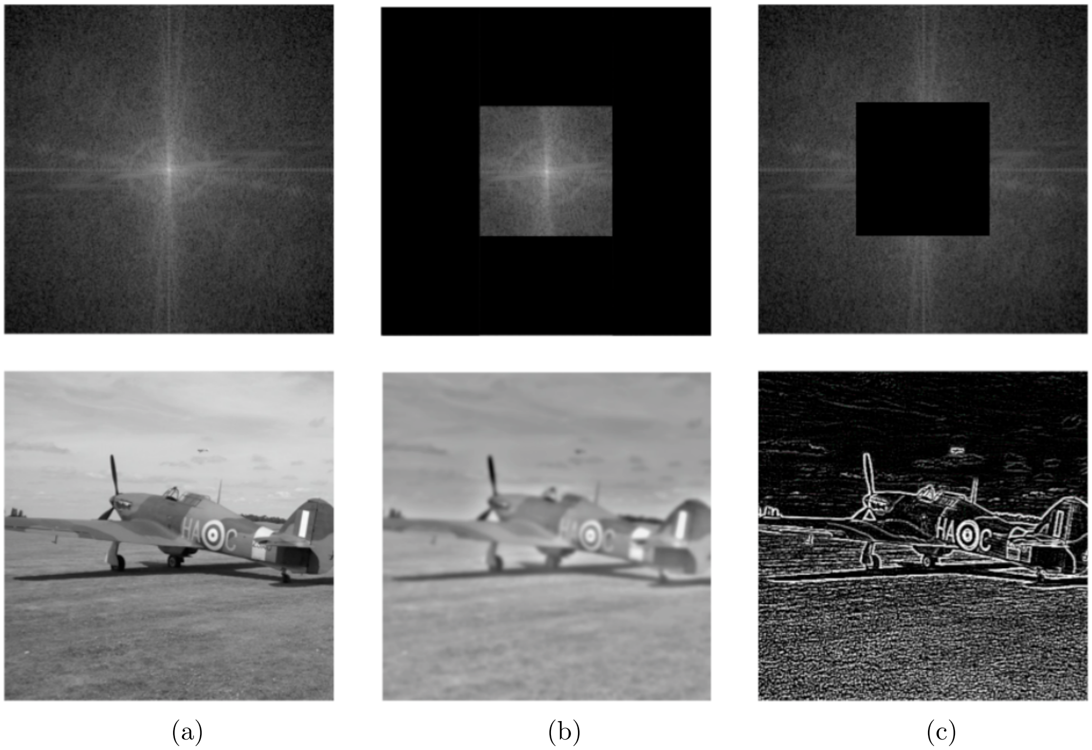

Figure 2.2: (a) The Fourier transform presented with its corresponding image. (b) A square aperture has been applied to the Fourier space of the image, blocking out all high frequencies. This causes the image to become blurry. (c) A square object has been used to filter out the low frequencies, resulting in a sort of trace of the image. Image credit: `http://practicalfmri.blogspot.ca/2011/08/physics-for-understanding-fmri_15.html`

2.2 Diffraction Limited Imaging

Now with our Fourier optics framework, we are equipped to discuss how light behaves when travelling through an aperture in a more general sense. When we were discussing filtering, we assumed that light was blocked by the aperture and the rest was transmitted without any change in behaviour. This works well in some cases, but it is helpful to do a more thorough treatment using the Fraunhofer approximation. One might wonder why not simply calculate the behaviour entirely (without approximations that is), however this quickly becomes increasingly complicated, and in most cases unnecessary. Hence, we will discuss Fraunhofer diffraction and apply it to our particular case of interest, the circular aperture.

2.2.1 Fraunhofer Diffraction

To start, we discuss the seemingly unrelated concept of the Fourier transform in the far field limit. In this case, if the propagation distance d is sufficiently long, we see that only plane waves with angles $\theta_x \approx \frac{x}{d}$ and $\theta_y \approx \frac{y}{d}$ will contribute to our amplitude. Hence, we see that this corresponds to a wave with spatial frequencies $\nu_x \approx \frac{x}{\lambda d}$ and $k_y \approx \frac{y}{\lambda d}$. This then means we have that

$$g(x,y) \approx \frac{i}{\lambda d} e^{-ikd} F(\frac{x}{\lambda d}, \frac{y}{\lambda d}). \tag{2.8}$$

This results in what is called the Fraunhofer approximation and it is evidently more accurate when d becomes larger.

Fraunhofer diffraction is a theory that states that uses the Fraunhofer approximation to determine that behaviour of the propagation of light after the aperture. In this case, for an incident wave with intensity $\sqrt{I_0}$, we write that right after the aperture

$$f(x,y) = \sqrt{I_0} p(x,y) \tag{2.9}$$

where $p(x,y)$ is called the pupil function and it is determined by the geometry of your aperture. In this case, out output function is

$$g(x,y) \approx \sqrt{I_0} \frac{i}{\lambda d} e^{-ikd} P(\frac{x}{\lambda d}, \frac{y}{\lambda d}) \tag{2.10}$$

where $P(\nu_x, \nu_y)$ is the Fourier transform of the pupil function. Hence, the intensity we would see would be given by

$$I(x,y) = I_0 \frac{1}{(\lambda d)^2} \left| P(\frac{x}{\lambda d}, \frac{y}{\lambda d}) \right|^2. \tag{2.11}$$

2.2.2 The Resolution Limit

Given Equation 2.11, we can calculate the resulting diffraction pattern for a variety of geometries. The one of particular interest is the circular aperture of diameter R with a corresponding pupil function given by

$$p_R(x,y) = \begin{cases} 1 & : \sqrt{x^2+y^2} \leq R \\ 0 & : \text{otherwise.} \end{cases} \tag{2.12}$$

For this function, we have

$$I(x,y) = I_0 \left[\frac{J_1(2\pi R r/\lambda d)}{(\pi R r/\lambda d)} \right]^2, \quad r = \sqrt{x^2+y^2} \tag{2.13}$$

where J_1 is the first order Bessel function. This intensity distribution is called the Airy pattern and the central peak is called the Airy disk. In particular, one will find that the angular position of the first minima is given by

$$\theta \approx 1.22 \frac{\lambda}{2R} \tag{2.14}$$

which corresponds to a spatial separation of

$$r = 1.22\frac{\lambda d}{2R}. \tag{2.15}$$

As a note, the numerical aperture NA is given by NA = f/d. As well, one will find that the full width at half max of this Airy pattern is given by

$$\mathrm{FWHM} = 1.028\frac{\lambda d}{2R}. \tag{2.16}$$

This applies directly to our understanding of the resolution of a system as the Rayleigh criterion gives the resolution based off of how far apart two point sources can be so as to remain distinguishable. This comes about through the diffraction of light throughout the system and so we say that the two points are resolved if

$$r \geq r_{\mathrm{min}}, \quad r_{\mathrm{min}} = 1.22\frac{\lambda d}{2R} \tag{2.17}$$

which is precisely the distance from the maxima to the first minima. Hence, two point sources have to be separated by a large enough distance so that their maxima do not lie inside of the others' minima.

Now, one can see from this equation that decreasing the aperture size makes the limiting distance larger which ends up lowering the resolution of the system. It also has the added effect of decreasing the total amount of light that reaches the camera, or sensor, which is generally detrimental.

2.3 Spherical Aberration

Two very common types of aberration are chromatic and spherical aberration. Since the imaging apparatus must be aligned for the one frequency of imaging light, chromatic aberration isn't a pressing concern. Spherical aberration, on the other hand, is a significant problem since it is inherent in almost all lenses. It is caused by the increased refraction of light rays that strike the outer regions of the lens compared to the center. This results in the rays focusing at different points depending on where they hit the lens as depicted in Figure 2.3.

One can mitigate this effect by using a complex system of lenses, a specially designed aspheric lens or an aperture. The aperture method is what will be used in this thesis as it doesn't require buying any costly components and is also relatively simple to implement. By placing the aperture at the Fourier plane, one can block the rays that aren't focused by at the focal plane. In principle, one can continue to aperture down until all but the perfectly focused rays are let through and hence get rid of all of the aberrations.

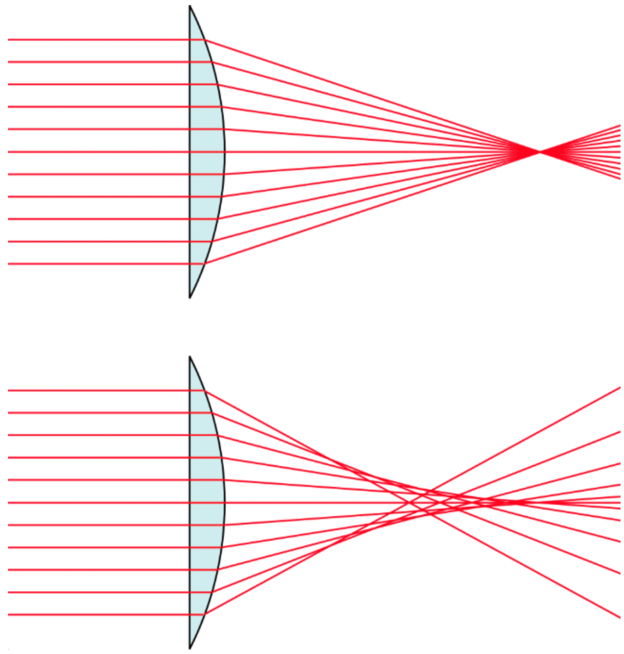

Figure 2.3: The top image is an example of what the rays would look like if there was no spherical aberration. The bottom image depicts a lens with spherical aberrations where the rays focus at varying positions along the horizontal axis.

In practice, there is some tradeoff between reducing the spherical aberrations and decreasing the resolution which will limit how much of the aberrations can be eliminated. This limit will be found experimentally and is one of the main aspects of characterizing the imaging system. In certain systems, one can forego this filtering to and attempt to correct for the spherical aberrations in the analysis, however it presents certain complications when looking at correlations in an image. This is because the distortion in the image will cause deviations away from the true intensity of the pixels, which then can cause false correlations to arise. This is particularly harmful when looking at small fluctuations in the image which is how one tests for entanglement as detailed in [4].

2.4 Fluorescence and Absorption Imaging

We will finish the chapter with a quick discussion of the two main types of imaging. The first, absorption imaging, revolves around the scattering of light away from the camera, which means objects cast a shadow. This shadow is then detected and based off of how dark it is, one can infer the density of the gas cloud at that location.

This is arguably the easier of the two imaging types, and it is also more frequently used as the subject can be moving while the image is being taken. While the versatility is a strong benefit, it is heavily dependent on the atomic scattering rate which is defined by

$$\Gamma = \frac{\Gamma_0}{2} \frac{\text{sat}}{1 + \text{sat} + (2\delta/\Gamma)^2} \tag{2.18}$$

where sat $= I/I_{\text{sat}}$ is a parameter which determines how close one is to saturation. This equation is simplified for our apparatus, where $(2\delta/\Gamma)^2 \approx 0$, sat ≈ 1 and $\Gamma_0 \approx 6$MHz for ^{6}Li. This means $\Gamma \approx 1 - 2$MHz.

Now, the signal to noise ratio, hereby denoted by SNR, goes like

$$\text{SNR} \propto \frac{\Gamma \cdot t \cdot \text{QE}}{\sqrt{A \cdot I \cdot t \cdot \text{QE}}} \tag{2.19}$$

where t is the exposure time, QE is the quantum efficiency of the apparatus, I is the intensity of the light, and A is the area of a particles possible position. Hence, for I being small, $\Gamma \propto \frac{\Gamma_0}{2}\text{sat}$ which means for $I = 2I_{\text{sat}}$

$$\text{SNR} \propto \sqrt{\frac{t \cdot \text{QE}}{A}}. \tag{2.20}$$

To increase the SNR, one could buy a very expensive camera to increase the QE, or one could increase the exposure time. Unfortunately, since Li is very light, the recoil from photon scattering generates a large velocity and therefore atomic drift. This will blur the image, which means there is an effective cap on the exposure time.

The alternative to absorption imaging is fluorescence imaging whereby atoms absorb light and re-emit it in a different direction. The emission light can be collected along an axis perpendicular to the illumination axis and the image will be bright if there is a high density. Since the intensity of the imaging light is weak, it needs to act on a relatively large timescale. This would also lead to atomic drift and so one must implement a pinning lattice to hold the particles in place. Then the limiting factor is the timescale on which atoms would heat out of the trap.

Fortunately, for zero field imaging, one can actually use either D1 or D2 light to simultaneously cool and image [7]. For low and high-field imaging, hyperfine splitting causes a difference between the cooling and induce spontaneous emission, which can then be imaged.

Chapter 3

Imaging System Design and Capabilities

Given the nature of the experiments we wish to conduct in the future, we aim to build an imaging apparatus that will image down the vertical axis and have a sufficiently high resolution. Equally important is the quality of image and hence a large part of this work is dedicated to reducing spherical aberrations. The reasons for the high resolution and lack of spherical aberrations are usual desires in a good imaging system. The orientation is mainly due to the orientation of our other trapping beams which cause a loss of intensity when doing high field imaging in a horizontal system.

3.1 Experimental apparatus

Before addressing the imaging system, it is important to understand the basic design of the experimental apparatus and hence what the imaging system must achieve. This information will motivate our overall design of the system and also outline its restrictions.

The main section of the apparatus is centred on the cell which is the container in which the particles are held. Above and bellow the cell are a pair of magnetic coils which provide an inhomogeneous magnetic field centred on the trap. Then as particles travel away from this centre, they're energy levels are shifted by the Zeeman effect.

As depicted in Figure 1.1, six MOT beams are directed at the cell which take advantage of the Zeeman shift to cool the particles in the cell. This works by a similar principle to the doppler shift, whereby particles moving towards the beams will have their energy levels shifted in such a way that they can be excited by the photons in these MOT beams. The beams have a frequency tuned such that particles with a low enough kinetic energy will not 'see' the photons in these beams and hence will remain undisturbed in the middle of the cell, whereas the particles moving towards the beams, and those not located sufficiently close to the centre, will be affected by the beams. These particles will absorb photons and radiate them in a random direction, meaning there is a net moment shift counteracting their movement. This causes the particles to simultaneously be cooled and localized in the centre of the cell.

A second beam, travelling along the vertical axis, called the IPG beam is responsible for the dipole trap. This beam has a narrow waist, and its interference along the vertical axis leads to

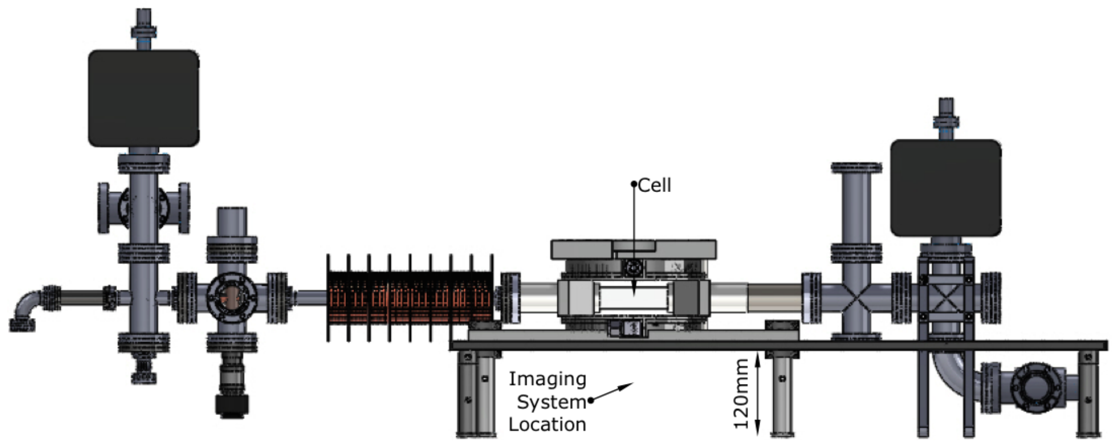

Figure 3.1: A 3D plan of the experimental apparatus. The cell location and area in which the imaging system is planned to be located are noted.

pancake-like potentials. These further localize the particles and provide stability. Along with the two MOT beams travelling along the vertical axis, the IPG beam and the imaging beam will also travel along the same axis and must subsequently be dealt with, to a certain degree, by the imaging system. Along with this comes the environment within which this apparatus is placed. This is detailed in Figure 3.1 and one can see that the spacing below the setup is limited. While it may be possible to build the imaging system above the apparatus it stands to reason that the stability of a system placed above the apparatus would be significantly lower than that placed below. As stability is highly relevant when one considers the quality of an image, this means the dimensions below the apparatus are yet another restriction placed on the design.

Considering now that this apparatus deals with atomic and molecular clouds on the order of 100μm, it is important to design the system with a wide enough field of view, depth of field and resolution to capture the cloud in its entirety. The field of view is set by the size of the CCD chip on the camera and the magnification of the system, while the depth of field and resolution are parameters determined by the lens and subsequent optical elements. In order to probe correlations between momenta in such a cloud, a resolution of approximately 2μm is required. While one might reasonably aim for a higher resolution, our apparatus is made for Li which is very light and hence travels very quickly. For an average exposure, a Li atom will drift approximately 2μm causing any further increase in resolution to be wasted.

Item Name	Part Name	Dimensions
Cell	Hellma UVH Cuvette	34 ± 0.5mm wide, 110 ± 0.5mm long
Aspheric Lens	Thorlabs AL5040-B	50 ± 0.1mm diameter, 15.5mm thick
Dichroic Mirror	Thorlabs DMLP900L	50.8mm diameter
Beam Cube		25.4mm side length
Camera	Apogee Alta U32	14.8mm×10.0mm imaging chip

Table 3.1: A table of the most crucial elements for the imaging system. The MOT beam focusing lens and mirror were omitted as they won't impact the imaging quality. The aperture and wave plate were omitted as they are flexible.

3.2 Imaging System Design

When designing the system, the major concern was how imperfections, causing errors like spherical aberrations, would impact the resolution of the system. The method we employed to deal with these spherical aberrations was to aperture down at the Fourier plane, effectively blocking the unfocused beams and recovering our original image. However, the placement of this aperture was uncertain as we were unsure, at the start, about the geometry and logistics of the system.

Before the process of designing the system is detailed, the final design will be presented here for two reasons; first to illustrate the basic layout of the system as changes were mostly made concerning the apertures location, and second to motivate the reasoning behind the design process. The design of the system is depicted in Figure 3.2, although the final distances between many elements have not been set here due to their dependence on later data. While not immediately apparent from this diagram, one of the main issues with the system is the spacing of the elements along the beam path. This system has to separate three beams, as depicted in Figure 3.3, and the MOT beam is approximately one inch in diameter when it originally hits the aspheric lens. This means that after two times the focal length, the MOT beam will return to this size.

As such, the optics must be located sufficiently close to the aspheric so as to encompass the entire beam or new, larger parts need to be purchased. If the MOT beam is clipped at some point, it will result in inhomogeneities in the trapping potential which ultimately lowers the quality of the trap. Considering this upgrade is taking place amongst many other projects, including the implementation of a Zeeman slower, the aim was to use components on hand to build the imaging system. Hence, it was decided to build the system as compactly as possible. As other systems are going to be implemented in the future, as described in Chapter 6, this has the added benefit of allowing for more flexibility with their implementation. The important components are listed in Table 3.1 along with their relevant dimensions. This can be misleading however as the mounts for many of these components make them significantly larger.

Returning to the design of the imaging system, the original idea was to place the aperture

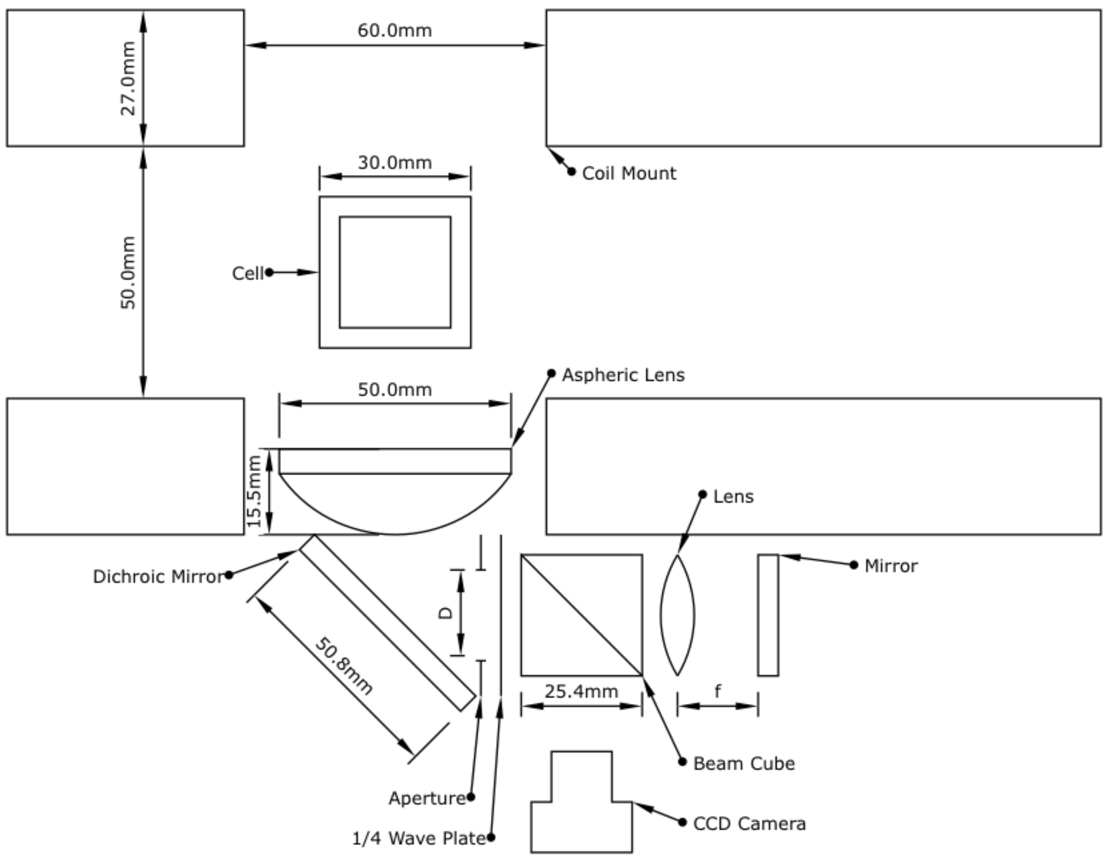

Figure 3.2: A rough mockup of the system. The distances between the cell, aspheric lens, dichroic and subsequent elements haven't been labelled as they change depending on the desired magnification. The optimal aperture diameter D will be determined experimentally. As well, the focal length of the lens for focusing the MOT beam onto the mirror is dependent on the specific lens we end up choosing.

between the aspheric and the dichroic mirror. As the aim was to filter at the Fourier plane, this would mean it would be 45.5mm away from the flat face of the dichroic because the reference location for the focal length was inset from the flat face by 5mm. Now, the dichroic was to be placed at a 45° relative to the vertical axis, which means that the beam will have to travel 35.92mm from top plane to the exit plane on the right. That leaves only 5mm in which to place the 1/4 wave plate, beam cube and focusing lens.

The next idea was to place the aperture between the cell and the lens, making only the beams that are close to the centre of the lens appear on the camera. These beams are subject to less spherical aberrations and this should result in a better quality of image. The main downside of this design is that it limits the usable area of the lens for beams coming through the dichroic. As will be evident in Chapter 6, the wider the diameter of the usable area, the better for our subsequent additions to this imaging system.

Finally the last design is the one depicted in Figure 3.2, where the aperture is place right after the dichroic lens. This has the benefit of condensing the system while also leaving the widest portion of the lens usable for beams passing through the dichroic mirror. Unfortunately, this means the beam will travel a total of 46.42mm before reaching the aperture. Therefore the aperture won't actually be placed at the Fourier plane and can result in some degradation of the image.

The amount of effect this will have on the image is unknown and this will be one of the tests that will be done in the characterization of this system. We next need to construct a 3D design of the imaging system so that parts can be manufactured. This also serves as another test that all of the geometries in the system will work. This was done in Solidworks using the drawing in Figure 3.1, and the main contraption is depicted in Figure 3.4.

In this design, the lens will be glued to the mount as the alignment will be vital to the overall capabilities of the system and we don't want it to drift over time. In order to ensure the lens is properly aligned throughout the entire process, a proper method would be to use the lens in an interferometer as done in [8].

3.3 Theoretical Capabilities

Given the brief review of Fourier optics in Chapter 2, we will henceforth develop a model upon which we will evaluate the effectiveness of our system. The first thing we must do is establish the method by which we will experimentally evaluate the imaging system. While using a gas cloud inside the cell might be the most indicative of how well our system will perform when the actual experiments are running, it will also make it very difficult to take measurements. In order to be accurate, we would need to build the system within the experiment and subsequently test its capabilities, however that would require that no experiments are conducted for a lengthy period of time. Therefore, we will use a pinhole of sufficiently small diameter to simulate our subject

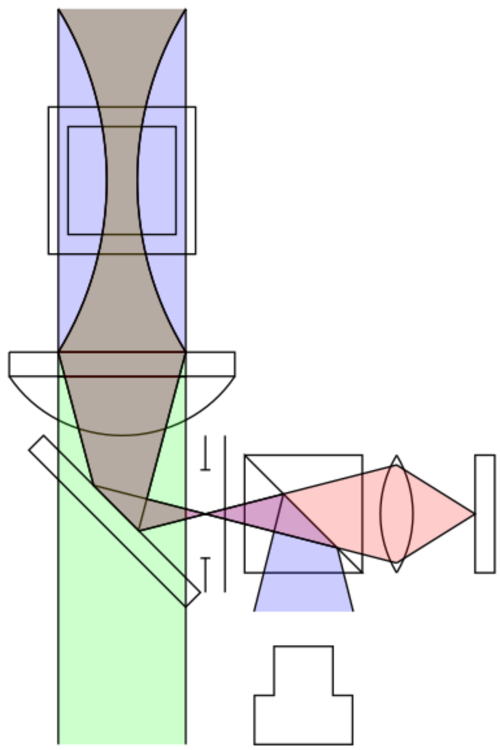

Figure 3.3: A depiction of the beam paths in the imaging system. The green beam is the IPG beam for the dipole trap and it is collimated by the aspheric lens. As it has a wavelength of 1064nm, it passes through the dichroic before being modified by optics not relevant to this work. The blue beam is the imaging light at 671nm. It subsequently reflects off of the dichroic mirror and due to its polarization, it also reflects from the beam cube towards the camera. Lastly, the red beam is the MOT beam which also reflects off of the dichroic and travels through the beam cube. The focusing lens and subsequent mirror are placed so that the beam is retroreflected.

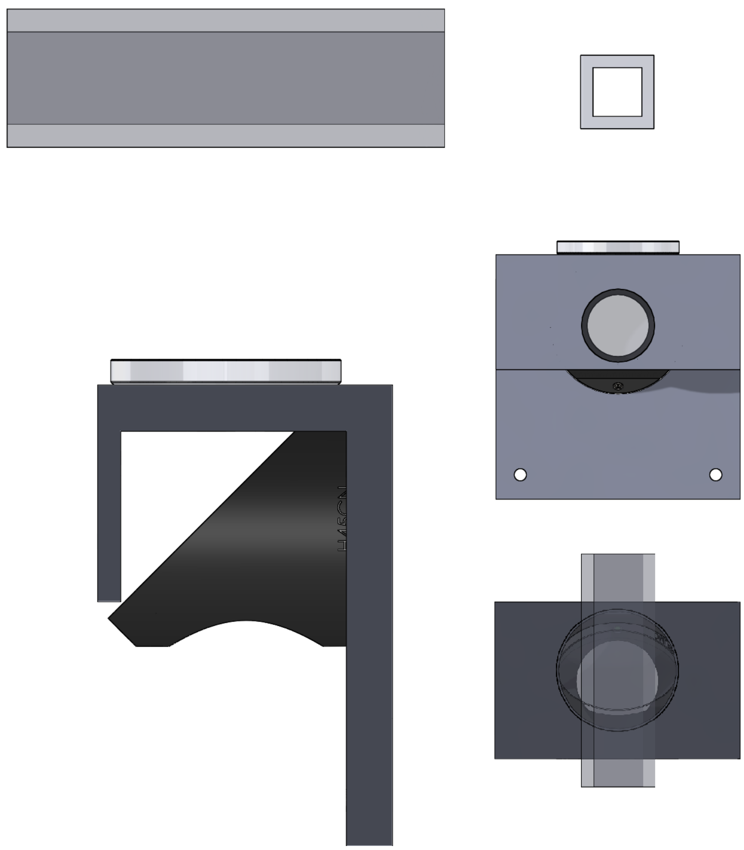

Figure 3.4: Solidworks drawing of the main components with the lens mount. The cell is depicted as being stationed above the entire mount with the lens resting in a round hole. Inside the bracket part is a Thorlabs H45CN 45° mount holding the dichroic mirror. This part will be modified by further milling out the base to have the access to the beam going through the mount. This entire setup will be mounted onto an L-bracket which will in turn be mounted on a 3-axis translation stage to provide adjustability along each axis. The lens will most likely be glued to the mount so as to improve stability.

matter. This pinhole must then have a size of approximately 2μm in order to be an efficient test of our system, and we have therefore used one with a diameter of 1μm.

Now, given this information, we can set out to construct our model. We start with the simplest model where we assume no diffraction occurs. In this case, the 1μm pinhole will be $M\mu$m in diameter on the camera where M is the magnification of the system. The image will be a clear disk which will be blurred by any spherical aberrations. In this case, changing the diameter of the aperture wouldn't do anything until a certain cutoff size, at which it would start filtering out the unfocused beams and the image would become clearer.

However, one can easily see that this model is overly simplified as the scale of distance between the camera and the aperture will be large enough to allow for significant diffraction from the aperture. If the magnification were sufficiently small one might see this behaviour, however the pixel size on the camera is 6.8μm×6.8μm and so a magnification of at least 7 would be needed to take up the majority of 1 pixel. With this magnification we see that

$$\begin{aligned} \frac{1}{f} &= \frac{1}{d_i} + \frac{1}{d_0} = \frac{1}{d_i} + \frac{M}{d_i} && (3.1) \\ &= \frac{1+M}{d_i} \geq \frac{7}{d_i} \\ \leftrightarrow d_i &\geq 7f = 280.0\text{mm} && (3.2) \end{aligned}$$

and we can expect diffraction to significantly alter our image at these length scales. Hence, we assume that the original 1μm pinhole image is diffracted by the aperture.

This is then modelled by taking the convolution of the *rect* function with the impulse response function which, in this case, is the Airy function. While one may be able to compute some analytic version of this convolution, it is sufficient, for our purposes, to numerically find the solution, the result of which is plotted in Figure 3.5 for a variety of diameters of the aperture. As you can see, when the aperture is wide, the output should look similar to the case where there is no diffraction, and if the aperture is small we converge to the Airy function.

Now, when we testing the imaging system, two very good measurements are the FWHM and the intensity of the image. If we change the aperture size and the intensity stays approximately the same, then we see that we haven't filtered any light. If we keep changing it and the intensity suddenly drops, it tells us the diameter at which we start filtering out the rays from spherical aberrations. Likewise, the FWHM is a measurement of how much diffraction is happening in our system and subsequently how the resolution changes as we change the aperture size. As such, the FWHM for the model is plotted in Figure 3.5 and the behaviour agrees with our understanding of diffraction.

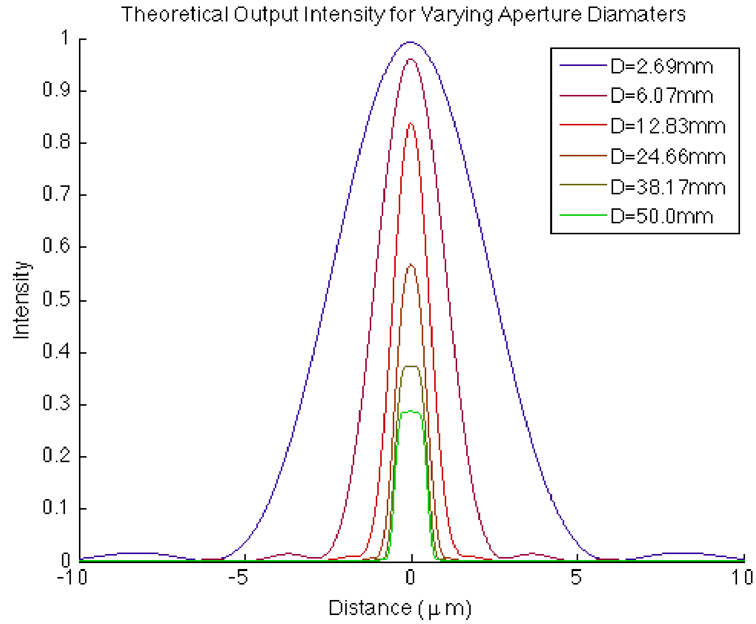

Figure 3.5: The end image intensity patterns for different aperture diameters based off of the theoretical model. The difference in intensity is unimportant and used to separate the curves visually.

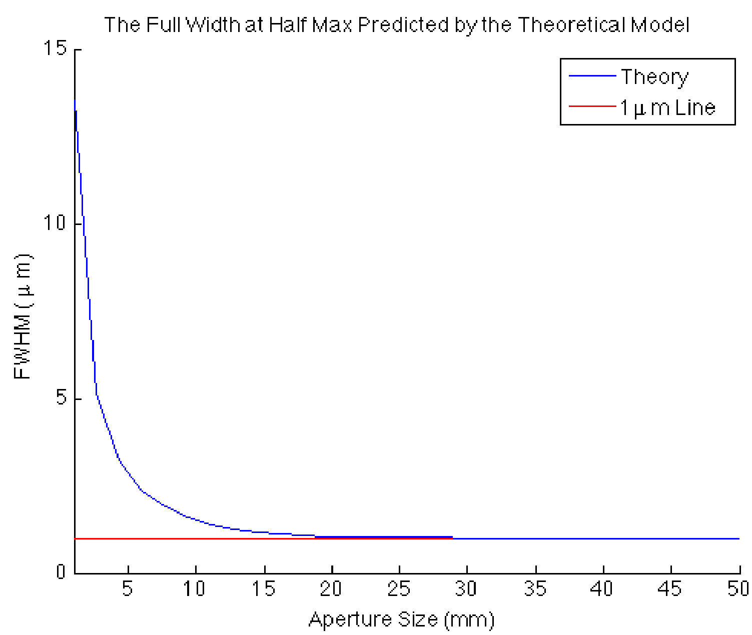

Figure 3.6: The FWHM predicted by the theoretical model for varying aperture diameter. A reference line at 1μm was included to further illustrate how the FWHM converges to 1μm as is expected.

Chapter 4

Data and Results

As was detailed in the previous chapter, the bulk of the characterization work was done by analyzing the trend in the FWHM and intensity of the image for a variety of apertures sizes. To understand how each element effected the image, this analysis was done for varying stages of completeness of the system. Before we analyze this data though, we must first touch on how we determined the magnification of the system.

4.1 Determining the Magnification

For simple experiments, one can use Equation 3.1 to determine the magnification by measuring the image distance d_i and the object distance d_o. However, without a very accurate measuring technique, this produces results with large uncertainties. To further complicate matters, the distance at which we measure the focal length from is inset from the surfaces of the lens, and the CCD chip in the camera is also inset. This would mean one would have to measure these distances accurately as well before calculating the overall distance, resulting in further errors.

An alternative to this method, would be to use a translation stage attached to the pinhole so as to translate it across the field of view. Using this method, translating the pinhole by some known amount results in the image being moved and one can then compare these distances to extract the magnification.

In order to do this accurately though, one must be able to determine the location of the Airy pattern within the image. This was done using a variety of scripts discussed in Appendix A. The centre of the peak was determined using a weighted mean of pixels with sufficiently high intensity so as to account for any random fluctuations that would otherwise skew the location of the peak. As in Figure 4.1, the data from the pinhole's translation and the relative positions of the peak were then fit to determine the magnification.

These values were then checked approximately using a measuring tape to make sure that they were realistic and that no error had occurred in the process.

4.2 Characterizing the Effects of Each Component

Given this rigorous method for determining the entanglement, we will now discuss the specifics of how the data was collected and analyzed before looking at the data for each stage of completeness.

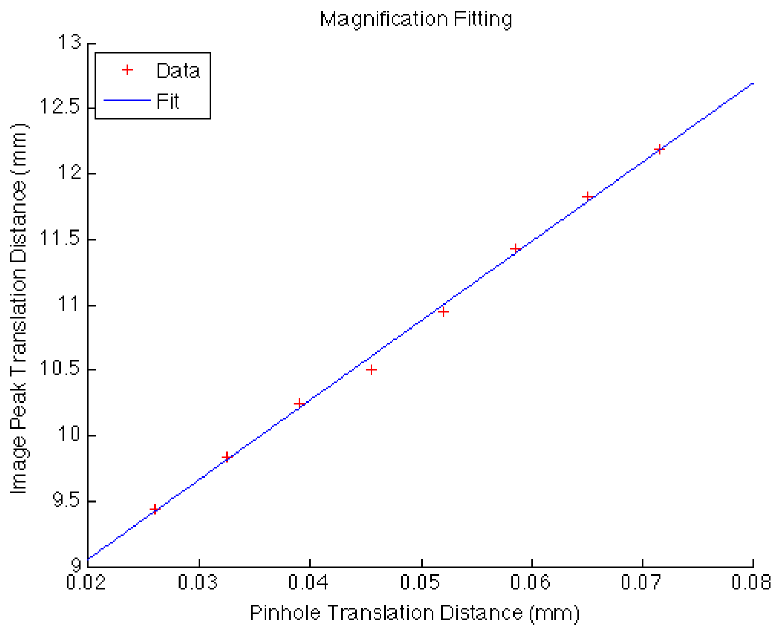

Figure 4.1: An example of the fitting process for the magnification data. This particular set came from the final setup.

The first step of the process was building, and aligning, the entire setup. With so few parts the assembly was trivial, however the alignment carried with it a wide variety of problems.

The most efficient way to build and align everything was centred around moving the pinhole in the plane parallel to the face of the lens, keeping the distance between the pinhole and the camera fixed. Then focusing would mean translating the lens along the beam's axis. Hence, the first thing was to place the lens camera at some fixed location, at which point the lens was placed on a translation stage at the appropriate height so that a beam would travel horizontally through the centre of the lens to the centre of the CCD chip. The pinhole was then placed on a 2D or 3D translation stage so that it could be translated to move it across the imaging plane. Lastly a laser source is placed behind the pinhole to provide imaging light.

At this point, one must align the system which involves different techniques for different distances. At a small distance between the pinhole and the camera, the depth of field is significantly larger so it is easiest to set the distance of the lens to the pinhole via direct measurement with a ruler, and then translate the pinhole in a systematic way so as to locate it. Then you can focus it more closely by taking a variety of images at different distances and comparing the resulting images' widths and peak intensities. Once the pinhole has been located and the image is focused, you can add the aperture at the focal length and the basic setup is complete.

If more components are needed, the same process would occur except the other components are to be added before one locates the pinhole. While they do complicate the system further, if one has kinematic mounts then there is yet another way to adjust the image's location.

Now, for a system with a relatively high magnification, one can take advantage of the fidelity of the human eye to find the pinhole. Using a relatively bright laser, on the order of 1mW, one can shine the beam through the system and locate it with one's eye. Since the power is bright enough, it is relatively easy to scan the area around where one estimates the pinhole image to be, and then adjust the system to place the image on the chip. Since the pinhole is so small, it filters out most of the power and thus the following this method will be safe. The benefit of doing this is that your eye has a variable focus that we can adjust innately, which makes it very easy to detect the beam, whereas the camera will have a hard time if the beam is out of focus.

Some alternatives to this method would be to use a significantly higher powered beam, and then if the image isn't focused there will still be enough light to give a wide range of focuses and one can then rely on setting the system up approximately. The consistency of this method depends on ones ability to approximately align the system based off of measurements, and can then vary significantly. Another method is to set the system up with a small magnification and use the appropriate method before slowly moving the camera farther away and adjusting the focus appropriately.

4.2.1 Setup Stage 1: Pinhole, Lens and Aperture

Arguably the most important component to characterize is the aspheric lens. As it has the most radical effect on the beams, it is the first aspect we characterize by making a very basic setup that consists of just the pinhole, light source, aspheric lens, aperture and camera. These are just placed along one axis and aligned as previously discussed.

Then, the aperture is opened to approximately 50mm, as the designed housing for lens won't give more space for the beam to travel through. A large number of pictures are taken at each aperture size so as to remove fluctuations during the analysis. A small selection of the images are given in Figure 4.2 to give an idea of the type of image we will analyze most of the time.

Now, our lens has a coating to reduce spherical aberrations for 780nm light and hence we would imagine it would follow our theoretical model more accurately than the data with 671nm light. We also took data for this wavelength and compared them both to the theoretical model in Figure 4.3.

We have plotted a total of 6 theoretical curves for the different wavelengths but also for varying sizes of pinhole as the pinhole we used has an uncertainty of 0.5μm in the diameter.

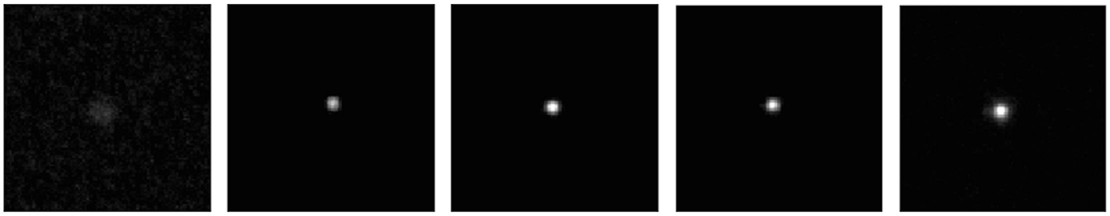

Figure 4.2: A selection of the images from the Stage 1 trials. From left to right they are; 10.04mm, 20.05mm 30.06mm, 39.91mm, and 49.92mm. Due to the small magnification, of approximately 25 times, the pinhole only shows up as a couple of pixels when the setup is focused and it is quickly lost when the aperture becomes too small.

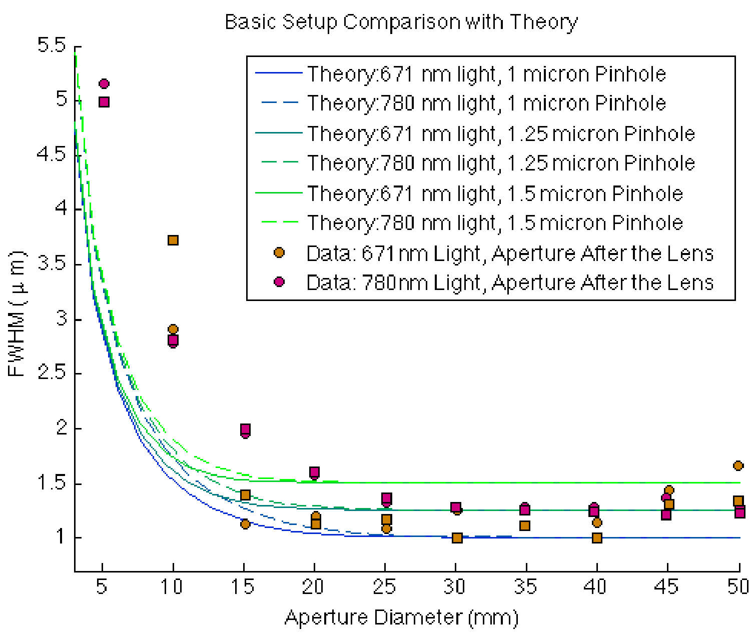

Figure 4.3: A comparison of the FWHM of the data at varying aperture diameters with what the theory predicts. This was done for 671nm and 780nm light and the corresponding theory curves. As there is an uncertainty in the pinhole's diameter, the curves were plotted for a pinhole size of 1.0, 1.25 and 1.50 μm. The circle markers are for the data along the horizontal axis, while the square markers are for the data along the vertical axis as shown in Appendix A.

We can see from Figure 4.3 that the data agrees with the model at large apertures but theres is some disagreement at lower apertures. This is most likely due to the fact we used the Fraunhofer approximation when modelling the diffraction caused by the aperture. It could also be that there are other sources of aberration that aren't accounted for by our model that are caused by the imperfections in the optics. Regardless, the FWHM of the pinhole image demonstrates our resolution is on the order of 1-2μm. This is the level or resolution we aimed for and so we wish to maintain this as we add subsequent components.

4.2.2 Setup Stage 2: Aperture Placed Before the Lens

Before testing more of the components, we wished to test the validity of the design with the aperture placed between the pinhole and the lens. Unfortunately, none of the apertures that were available had a large enough range of diameters while being slim enough to fit between the pinhole and the lens. To circumvent this problem, a variety of aperture sizes were cut out of a hard card paper and attached to the lens mount.

While the two data sets in Figure 4.4 seem to flatten out at diameters greater than 20mm, the aperture before the lens has a significantly worse resolution. Assuming that the subsequent additions to the system will further reduce the resolution, placing the aperture before the lens was eliminated as an option for this reason. We can further support this choice by looking at how the intensity falls off in Figure 4.5.

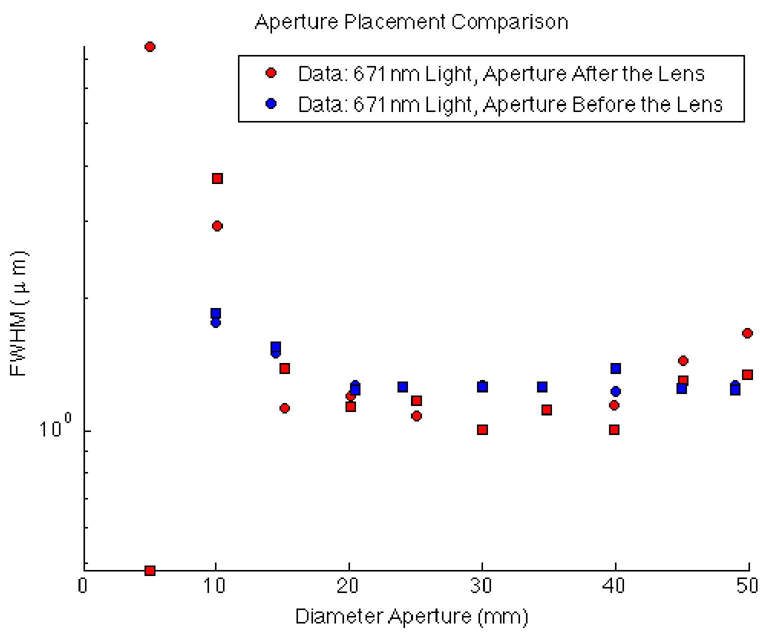

Figure 4.4: A comparison between the designs with the aperture placed before and after the lens. The anomalous data point at 5mm is due to an inability to fit the data because the amplitude of the noise was comparable to the image intensity.

We can see that the intensity falls off slower for the design with the aperture placed before the lens which means that we don't filter out as much spherical aberration for the same amount of aperture change. This leads to having to use a smaller aperture in order to achieve the same amount of filtering which in turn drops the resolution further. Hence, the design with the aperture placed after the lens is the best choice and we test the rest of the optics to discern how the final imaging system will transform the image from the pinhole.

4.2.3 Setup Stage 3: Addition of the Cell

The last test before the entire setup is to test each side of the cell to make sure it has the same behaviour on each side. This would also confirm that the cell walls are all the same and are also sufficiently flat which means that the choice of cell orientation is unimportant. While this isn't necessarily required for the imaging system, at least two opposing sides would need to be tested. This information is summarized in Figures 4.7 and 4.8.

It is important to note that at this point the setup had been changed to have a magnification of approximately 85 times due to the availability of space. This allowed us to better focus the image, as well as fit the data more accurately as the image takes up more pixels. To illustrate, a selection of images are placed in Figure 4.6. The angular symmetry is particularly important as well as the similarity to an airy pattern.

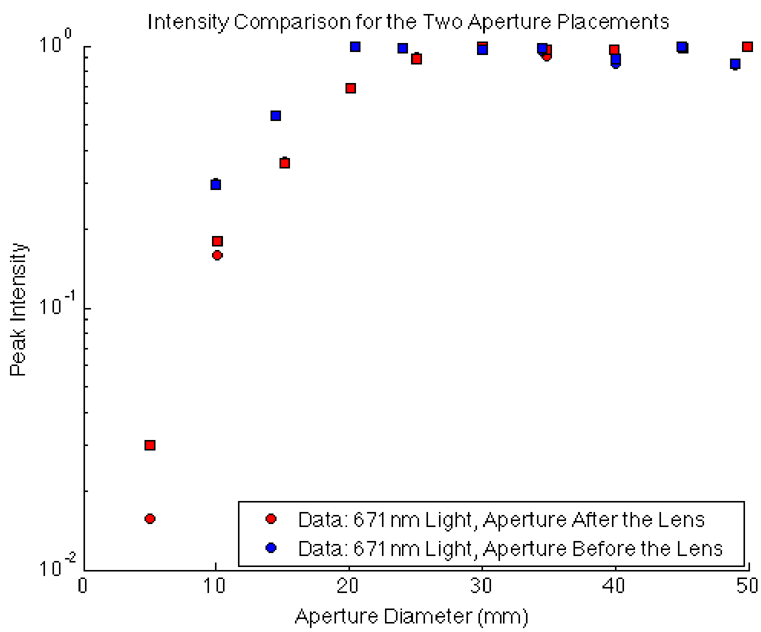

Figure 4.5: A comparison between the intensity of the designs with the aperture placed before and after the lens.

It is evident from these plots that all four sides are very uniform in how they transform the image. There is a slight deviation in Figure 4.7 in the 15-20mm aperture range, however they are otherwise fairly consisted.

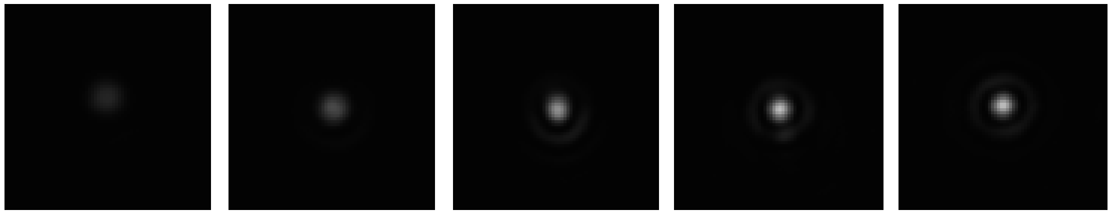

Figure 4.6: A selection of the images from the Stage 3 trials. From left to right they are; 11.04mm, 14.06mm 17.02mm, 20.04mm, and 35.07mm. Notice the radial symmetry and the clear ring in the later images that are indicative of diffraction.

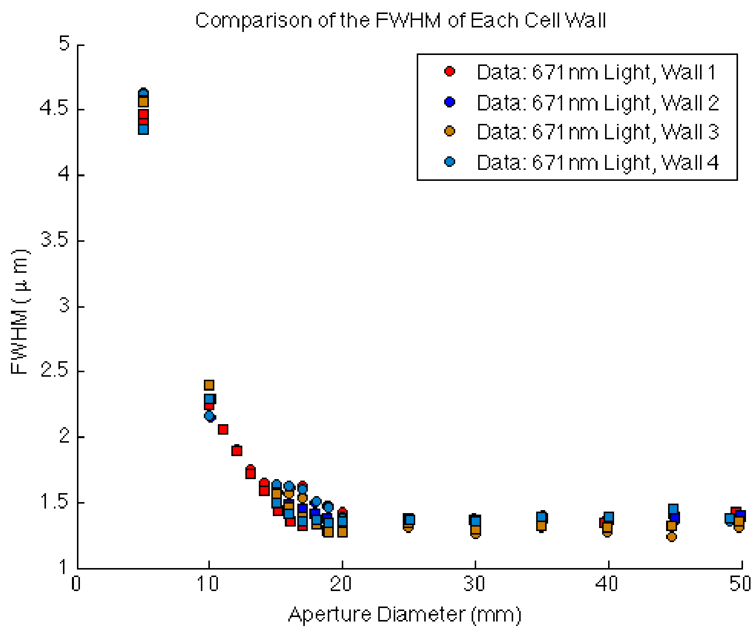

Figure 4.7: A comparison of the effects of the four cell walls on the FWHM of the pinhole image.

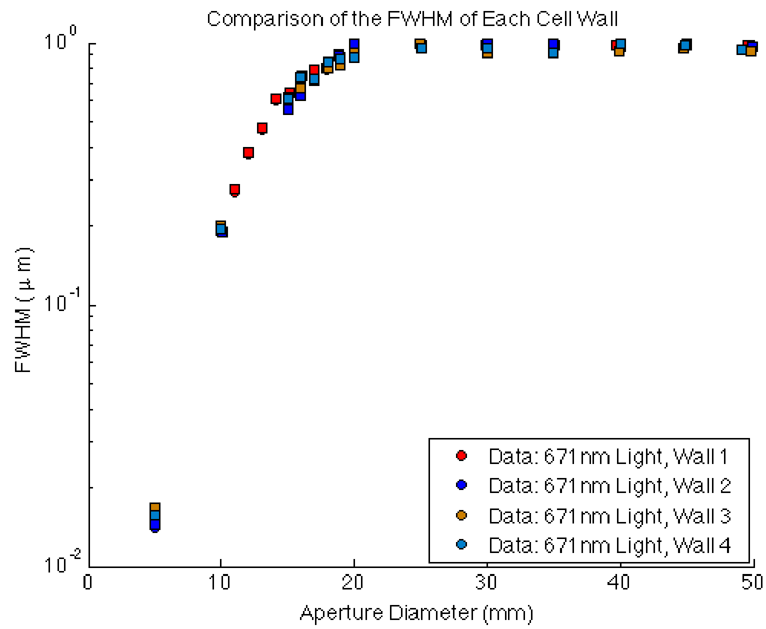

Figure 4.8: A comparison of the effects of the four cell walls on the intensity of the central peak of the pinhole image.

4.2.4 Setup Stage 4: Final Setup

For the final setup we did two tests. The first was with all the parts assembled and with the aperture placed at the Fourier plane. This served to address how all of the optical elements transformed the image and hence it was the main characterization of all the components.

The second test was for the aperture placed 6mm past the Fourier plane as is dictated by the design and geometry of the setup. This would characterize the final design as a whole and hence be the main result. Before getting to the data, we note here that the pinhole we had been using for the previous tests had been damaged and therefore replaced. This could mean that the new pinhole was actually a different size and result in the tests giving a different resolution. However, as these tests only set an upper bound on the resolution, the two data sets can still be used together to understand how the system behaves.

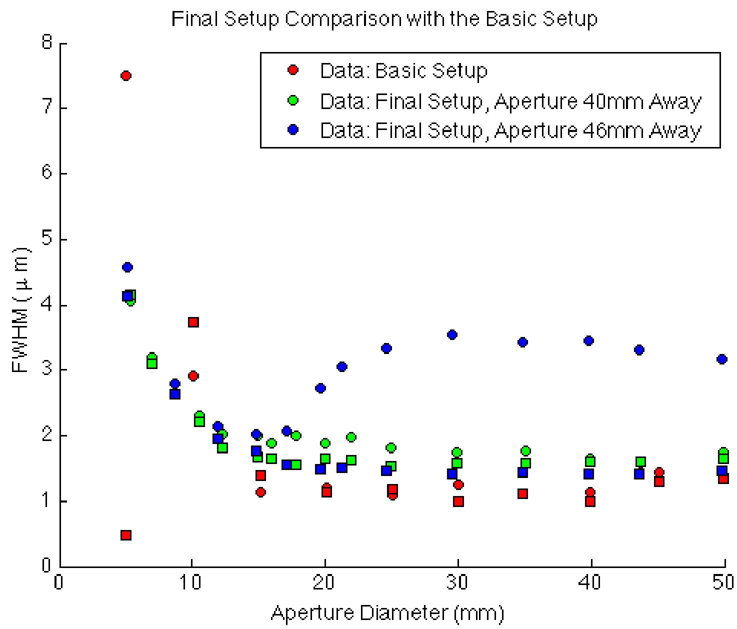

Figure 4.9: A comparison of the basic setup, the final setup with the aperture at the Fourier plane and the final setup with the aperture placed 6mm past the Fourier plane. The disagreement between the horizontal and vertical data sets for the aperture placed away from the Fourier plane is indicative the asymmetry in the image.

Returning to the actual data, the results are plotted in Figures 4.9 and 4.10 along with the original data from the basic setup to compare how the addition of the other optical elements affected the image quality.

If we first look at Figure 4.10, we see that all three data sets look fairly similar. The apparatus with the aperture at the Fourier plane (40mm away from the lens) is very close to the basic setup, though the main difference is that it starts curving closer to 15mm. The setup with the aperture 46mm away has a gentler slope than the other two data sets and it looks as though it might start curving around 18mm.

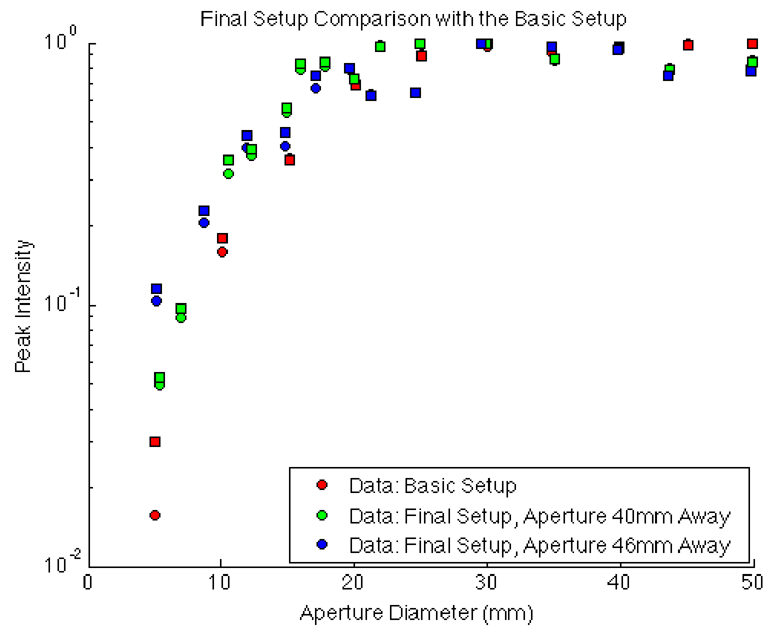

Figure 4.10: A comparison of the basic setup, the final setup with the aperture at the Fourier plane and the final setup with the aperture placed 6mm past the Fourier plane.

However, if we look at Figure 4.9 we see a very different picture. Arguably the most striking feature is the difference between the horizontal and vertical values for the data at 46mm away. This is indicative of some asymmetry in the image that we shall discuss shortly. Putting aside this asymmetry, we see that the 40mm and 46mm data sets agree well with one another. Their curvature is much more gradual than the that of the basic setup but it looks like it starts curving anywhere from 15mm to 20mm.

Overall though, it seems to have a lower resolution, even after one compensates for the difference in pinholes. While this is unfortunate, the data still shows that the resolution is better than the 2μm goal. Hence the next major concern is this asymmetry that seems to only be present in the 46mm data. For this we look at Figure 4.11 which compares some of the images from the 40mm data set with those in the 45mm one.

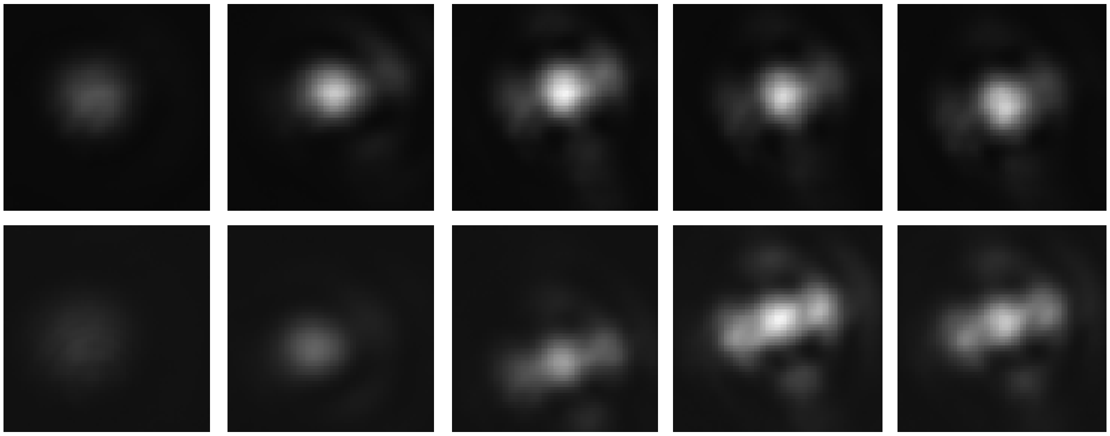

Figure 4.11: A selection of the images from the Stage 4 trials. From left to right they are; 10.51mm, 15.98mm 22.0mm, 35.13mm, and 49.92mm. Notice the striking asymmetry from the bright axis at approximately 30° to the horizontal.

From both sets of images, it is clear that there is some asymmetry causing a brightening of an almost horizontal section of the image. It is unclear why it is more dramatic in the 45mm data set, especially when the aperture is open to almost 50mm. Looking again at Figure 4.6, we see that this asymmetry wasn't present, indicating that the source is most likely one of the new optical elements. Hence we proceed to diagnose this problem.

The first check is to make sure that nothing had happened to the lens that would cause this asymmetry. An easy test for this is to rotate the lens and see if the asymmetry also rotates. This was done and the results are shown in Figure 4.12.

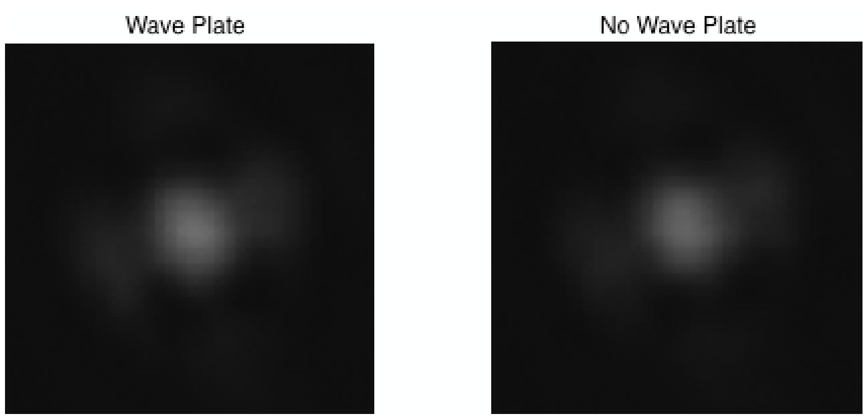

Figure 4.12: A comparison of the asymmetry before the lens was rotated by ~ 90° and after. Notice how the main bright asymmetry remains at the same location indicating that the lens is not the problem.

The bright line remains at approximately the same angle which suggests that it is one of the other components that is causing the asymmetry. The next component to test is the wave plate. Since rotating the wave plate would cause a significant lose in intensity due to the beam cube, it was instead removed to see if the asymmetry was resolved. This is shown in Figure 4.13 and again both images are almost identical. Hence the only components left to test are the dichroic mirror and the beam cube.

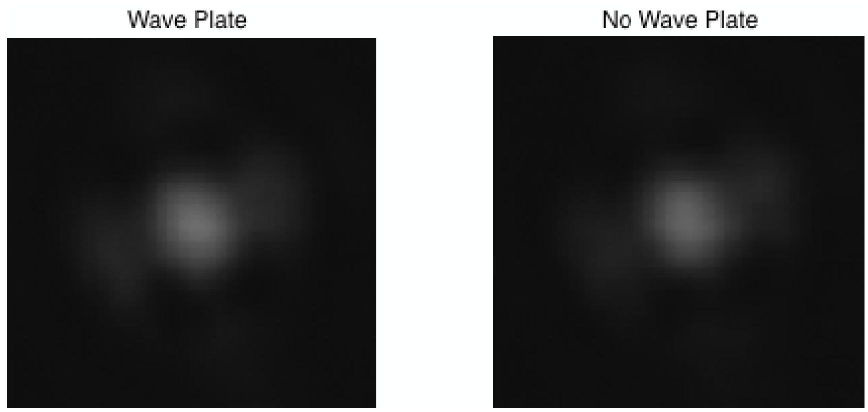

Figure 4.13: A comparison of the asymmetry before the wave plate was removed and after.

Due to alignment issues, the rotation of the dichroic changed the image, causing other more pronounced aberrations. As such, we are left with the dichroic mirror, beam cube or an unknown source of aberration. Unfortunately, due to the system's design, it is not trivial to rotate or remove the beam cube and hence this final test wasn't conducted as a part of this thesis. It will be much more simple to resolve while actually installing the apparatus in the main system and will be done at that time.

Chapter 5

Entanglement Theory

One of the major motivations for building this high resolution imaging system is that it would allow for the study of entanglement through density correlations, the details of which are in Section 5.2. Some recent papers [1, 2] have examined the entanglement, in momentum space, of a degenerate quantum gas which would be within our realm of possible tests. This is of particular interest as ultra-cold gases provide a relatively noise free environment within which one can examine many-body entanglement and it would be beneficial to develop those techniques further. To this end, the imaging apparatus was designed with these measurements in mind and therefore it is appropriate to discuss these ideas and how one might measure them in a similar apparatus.

5.1 The Density Matrix and the Entanglement Entropy of a System

Before addressing entanglement directly, it helps to review the density matrix formalism and how entanglement is expressed in this form. Hence, to start we first examine Bell states as an introductory example.

One of the fundamental two qubit states in quantum computation is given by

$$|\psi\rangle = \frac{|00\rangle + |11\rangle}{\sqrt{2}}. \tag{5.1}$$

Now, given an unentangled two qubit state, say $|\Phi\rangle$, one would be able to decompose it into a product of two qubits, i.e. there exists some single qubit states $|\phi_1\rangle$ and $|\phi_2\rangle$ such that $|\Phi\rangle = |\phi_1\rangle|\phi_1\rangle$. It is in this way that we define an entangled state. We say a state $|\Phi\rangle$ is entangled if there are no such states $|\phi_1\rangle$ and $|\phi_2\rangle$ such that $|\Phi\rangle$ is their product.

Alternatively, instead of building quantum mechanics using state vectors, one can use the density matrix instead. It provides a much nicer way of expressing individual subsystems of a composite system which is helpful when dealing with entanglement. As such, when discussing a quantum system whose state isn't completely known, we describe it by the possible states $|\Phi_i\rangle$, which it could occupy, and their respective probabilities p_i. In this language the set $\{p_i, |\Phi_i\rangle\}$ is called an ensemble of pure states and the corresponding density operator is defined as

$$\rho = \sum_i p_i |\Phi_i\rangle\langle\Phi_i| \tag{5.2}$$

with an analogous density matrix

$$\rho_{jk} = \sum_i p_i \langle e_j | \Phi_i \rangle \langle \Phi_i | e_k \rangle \tag{5.3}$$

for some basis $\{|e_i\rangle\}$.

In this way, we can describe the evolution of the density operator by the unitary operator $\hat{U}$ by

$$\rho \xrightarrow{\hat{U}} \hat{U}\rho\hat{U}^\dagger. \tag{5.4}$$

The density operator has a rather large number of nice properties like

i) $\mathrm{tr}(\rho) = 1$,

ii) $\langle\psi|\,\rho\,|\psi\rangle >= 0$.

It is important to note that this means that the density operator permits a spectral decomposition. There are a variety of other useful properties that we will skip, however one will find a much more thorough description in Chuang [9]. Turning now to how the density operator describes subsystems of some composite quantum system, we will have to discuss the partial trace and the reduced density operator.

Suppose now, there are two physical systems labelled A and B with a corresponding density matrix ρ^{AB}. If now we wish to focus solely on subsystem A, we define the reduced density matrix for system A as

$$\rho^A = \mathrm{tr}_B(\rho^{AB}) \tag{5.5}$$

where the partial trace is defined by

$$\begin{aligned} \mathrm{tr}_B(|a\rangle \langle a'| \otimes |b\rangle \langle b'|) &= |a\rangle \langle a'| \,\mathrm{tr}(|b\rangle \langle b'|) \\ &= |a\rangle \langle a'| \langle b' |b\rangle . \end{aligned} \tag{5.6}$$

Therefore, if $\rho^{AB} = \rho^A \otimes \rho^B$, then our notion of the reduced density matrix is consistent since

$$\rho^A = \mathrm{tr}_B(\rho^{AB}) = \mathrm{tr}_B(\rho^A \otimes \rho^B) = \rho^A \mathrm{tr}(\rho^B) = \rho^A. \tag{5.7}$$

Before addressing entanglement directly, we will discuss the entropy of a quantum state. Following the Shannon entropy from information theory, we have the von Neumann entropy $S(\rho)$ defined as

$$S(\rho) = -\mathrm{tr}(\rho \log_2 \rho) \tag{5.8}$$

where we define $0\log_2(0) = 0$. For a pure state, we have that $\rho = |\psi\rangle\langle\psi|$ for some state $|\psi\rangle$ and hence the von Neumann entropy will be zero. On the other hand, an entangled state will have a non-zero entropy. In fact, a maximally entangled system will have $\rho = I/d$ where d is the dimension of the density matrix. It is hence by the definition of the von Neumann entropy, or entanglement entropy as it is sometimes called, that we define the entanglement of a system. A system can have an entanglement entropy in the range of 0 to $\log_2 d$ and it is zero if and only if it is unentangled or a pure state.

We can also look at the entanglement entropy of some subsystem using the reduced density matrix, whereby

$$S_A = -\mathrm{tr}(\rho_A \log_2 \rho_A) \tag{5.9}$$

provides a measure of the entanglement between A and the rest of the system.

5.2 Motivating Theory and Measurement Scheme

As has been previously mentioned, this system was designed in hopes of performing some momentum space correlation measurements. In particular, it was theorized that the entanglement entropy in momentum space is zero in the ground state before diverging in the continuum limit. Furthermore, the density matrix can be explicitly calculated and hence, by measuring the correlations between different momentum space modes, one can easily compare the theory to experimental results.

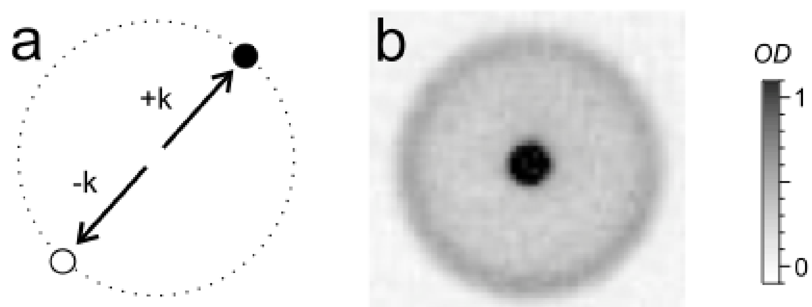

Figure 5.1: (a) Due to momentum conservation, if a stationary molecule decays into two atoms, they must have equal and opposite momenta. Therefore, they would be found on opposite sides of the atomic cloud. (b) An absorption image after the dissociation of weakly bound molecules. Notice the clear ring demonstrating the momentum correlations. The small, dark dot is caused by the molecules that didn't dissociate and therefore remain at the centre, blocking light. Figure from [6].

In order to conduct these measurements, we will take a time-of-flight (ToF) measurement. This involves releasing a trapped gas and imaging it after it has expanded. If it has expanded to be much larger than the original cloud of particles, we say that the spatial density distribution approximates the momentum distribution.

To illustrate this idea, let us begin with an atomic cloud in some initial state $|\Psi(t=0)\rangle$ with a width of L. Once it is released it will evolve according to the unitary operator

$$\hat{U}(t) = \exp\left(-it \int \frac{dk}{2\pi}\omega(k)\hat{n}(k)\right) \tag{5.10}$$

and subsequently we look at the time evolution of the field operators $\hat{\psi}(x)$, $\hat{\psi}^\dagger(x)$.

We then see that

$$\hat{\psi}^\dagger(x,t) = \hat{U}^\dagger(t)\hat{\psi}^\dagger(x,0)\hat{U}(t) \tag{5.11}$$

$$= \int_{-\frac{L}{2}}^{\frac{L}{2}} d\tilde{x}\ \hat{\psi}^\dagger(\tilde{x},0)\left[\int \frac{dk}{2\pi}e^{i[k(\tilde{x}-x)-\omega(k)t]}\right] \tag{5.12}$$

where we then integrate the piece in the square brackets explicitly. Note that this integration only works when we give the time a small imaginary part. This gives us

$$\mathcal{I}(x,t) = \int \frac{dk}{2\pi}e^{i[kx-\omega(k)t]} \approx \sqrt{\frac{m}{2\pi it\hbar}}e^{i\frac{mx^2}{2t\hbar}} \tag{5.13}$$

We can then ask, how long does it take for the separation between the initial momentum states to become larger than the initial size L of the system? To answer this we look at the commutator

$$[\hat{\phi}_k, \hat{\psi}^\dagger(x,t)] = \int_{-\frac{L}{2}}^{\frac{L}{2}} d\tilde{x}e^{-ik\tilde{x}}\mathcal{I}(\tilde{x}-x,t) = \tilde{\mathcal{I}}_k(x,t) \tag{5.14}$$

After some manipulation, we get

$$\tilde{\mathcal{I}}_k(x,t) \approx \sqrt{\frac{m}{2\pi it\hbar}}\exp\left(i\frac{mx^2}{2t\hbar}\right)\frac{\sin\left(\frac{mxL}{2t\hbar}\right)}{\left(\frac{mx}{2t\hbar}\right)} \tag{5.15}$$

where we have assumed that $x >> \frac{L}{4}$ which means the wave packet has spread a large amount compared to the cloud's initial size L. Following that, we can identify that this describes a function of width $W = \frac{2\pi t\hbar}{mL}$ but our initial approximation requires that $W >> \frac{L}{4}$ which means that the expansion time is $t_{\text{TOF}} >> \frac{mL^2}{8\pi\hbar}$. For a trapped Li cloud of size 20μm, we find that $t_{\text{TOF}} >> 1.5$ms.

Now, ff this is not the case, we have a new function with width $W \approx \frac{L}{2}$. Regardless, we see that the each initial momentum, $\hbar k = \frac{2\pi\hbar l}{L}$ for some integer l, is associated with a density distribution centred at $x = \frac{\hbar kt}{m}$ with width W. Thus each initial momentum is well resolved when $W << \frac{2\pi\hbar t}{mL}$.

This happens at a time when the width of the initial cloud has a negligible effect on the width of the cloud after expansion, which we find to be $t \approx \frac{mL^2}{2\pi\hbar}$ which is on the order of 1.5ms for ^{6}Li. Thus, if we let the cloud expand for some time longer than this, we will be able to fully resolve the momentum distribution.

Since we can then relate the density distribution with the momentum distribution, the intensity of a pixel on the camera will translate to the number of particles at with that momentum.

Then, given a particular momentum mode, one can ask what is the likelihood of finding a particle at some other momentum state. In this way, we can construct these correlations between momentum modes and then compare with theory. These types of experiments have been previously carried out and this results in images like the one shown in Figure 5.1.

Chapter 6

Future Considerations

Considering the imaging system has a sufficiently high resolution, the next step is to address this asymmetry. Most likely, it is due to some imperfections in the dichroic or beam cube and should therefore be relatively easy to correct. Once this is completed, it would be useful to characterize the imaging system's field of view and how the image quality changes over the surface of the lens. This might be more easily tested once the imaging system is installed as one could conduct an experiment similar Jin's [6]. This would be helpful because the image is very well understood and it would utilize the whole lens. Hence, any aberrations in the image would be evident. As such, once the source of the asymmetry is found, the next step might be to install the imaging system in the main apparatus and conduct the such an experiment.

Also mentioned previously was the desire to implement a pinning lattice for fluorescence imaging. While fluorescence imaging can't be used for the entanglement measurements we have mentioned, due to the nature of ToF measurements, it is the ideal form of imaging for many other experiments. This wouldn't require much extra testing and would allow for a wide range of new experiments.

6.1 Dilating Lattice

An interesting extension of this lattice technology is, what we have called, the dilating lattice. It would be a great compliment to a pinning lattice and it would serve to further upgrade our imaging system in situations where you can hold your gas in a lattice. What it will do, instead of increasing the resolution of the imaging system, is increase the spacing between the subjects of interest. This leads to a decrease in the required resolution and will therefore allow our imaging apparatus to perform comparably to many other quantum gas microscopes.

While it is unfortunate that the dilating lattice can only be used in certain circumstances, many quantum gas microscopes use similar scheme to boost the resolution of the system. These can range from a solid immersion lens [5], which require the gas to be confined to a plane close to the lens, to a complicated set of lenses [10, 11], which are costly and very difficult to align and maintain.

Now, before we discuss the design, it is important to note a couple of drawbacks to this method. While it will cost significantly less than many other quantum gas microscopes, it won't have the ability to address single sites in situ. While this won't necessarily be a problem for many of the experiments we aim to conduct, it nevertheless presents a bound on what one might explore with this apparatus. Similarly, it also requires that the particles be held in this lattice which may not be ideal for some experiments. In this case, one would have to solely rely on the resolution from the imaging apparatus. That said, the system will provide many benefits but we will first examine the basic concept behind the lattice and what it can be used for.

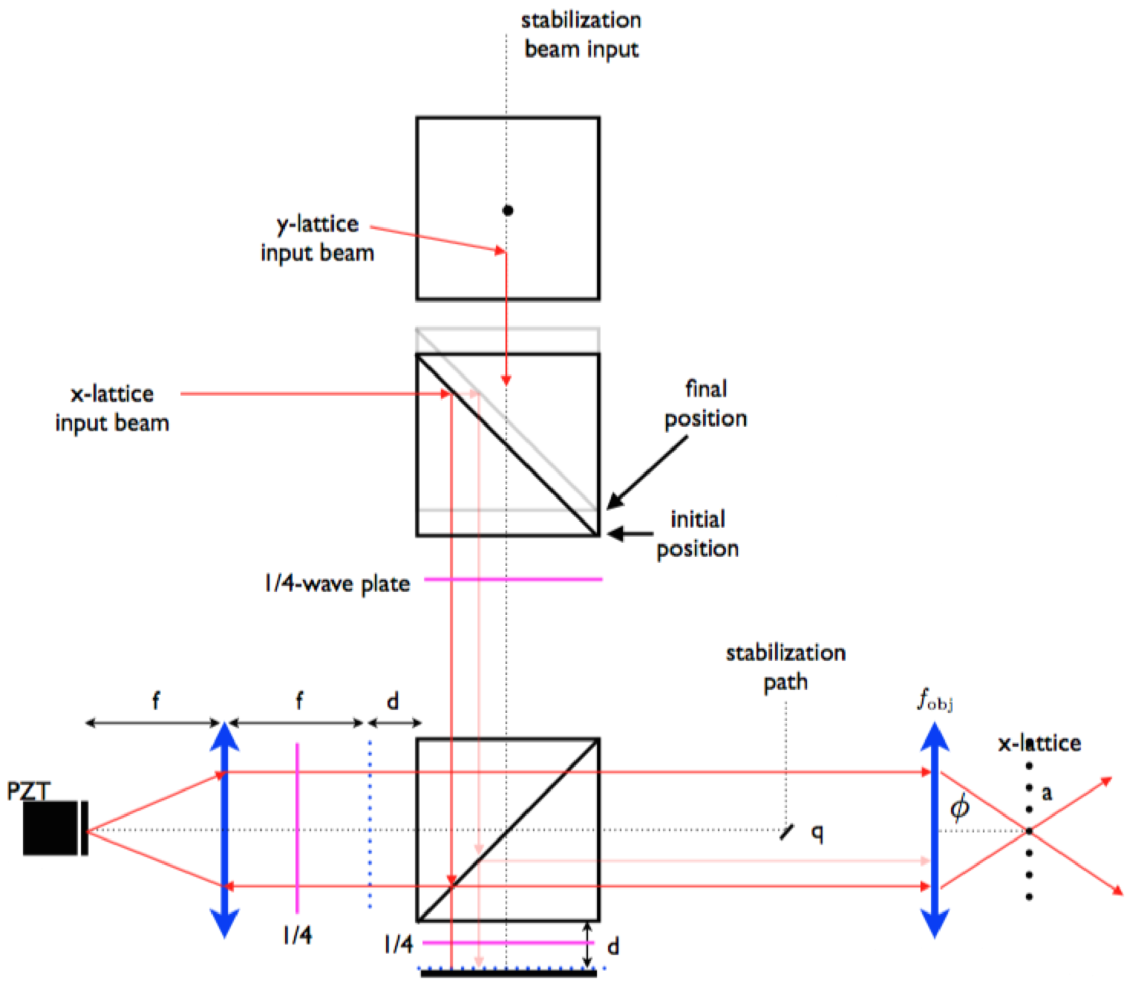

Figure 6.1: A rough sketch of the dilating lattice apparatus. The middle beam cube can be translated along the vertical axis and it generates two parallel beams of varying separation. The stabilization path is essentially an interferometer which will allow for the adjustment of the relative path lengths to stabilize the lattice.

The apparatus is depicted in Figure 6.1 and it takes a single input beam and transforms it into two, parallel output beams. The separation of these output beams is dictated by the location at which the input beam reflects from the beam cube. This location can be changed by translating the beam cube along the vertical axis, which means the beam separation is easily changed in a mechanical manner. This is important because all the rays will focus at some distance f past the lens, meaning the shift in separation changes the angle ϕ at which the rays are focused. These beams then cross at the focal length, causing interference and hence a lattice potential.

The lattice spacing is given by

$$a = \frac{\lambda}{2\sin(\phi)} \tag{6.1}$$

and so, by changing the separation of the beams one can change the lattice spacing. What this means is one can load the dilating lattice when it is expanded, contract it so that tunnelling between lattice sites can occur, and then expand it again to image each site. The bounds on the sizes of the lattice are

$$a_{\mathrm{min}} = \frac{\lambda}{2\mathrm{NA}} \tag{6.2}$$

$$a_{\mathrm{max}} = \frac{\lambda f_{\mathrm{obj}}}{2q} \tag{6.3}$$

where NA is the numerical aperture of the lens, and q is the size of the small mirror for the stabilization path. Since the main object will be the aspheric used in the imaging apparatus, these bounds are $a_{\mathrm{min}} \sim \lambda$ and $a_{\mathrm{max}} \sim 5\lambda$ using a $q \approx 5$mm. Hence, if one uses 522nm light, this would result in a compressed lattice space of approximately 0.5μm and an expanded lattice spacing of approximately 2.5μm. This can be resolved using the imaging apparatus.

This would be a viable method for increasing the resolution of the imaging apparatus. Another application is for trap loading, whereby one loads the gas cloud into the expanded dilating lattice, contracts the lattice and then transfers the particles into a dipole trap. Currently, when loading the dipole trap with a 100μm cloud, one will typically fill a large number of 'pancake' potentials as depicted in Figure 6.2. If, instead, one were to load it into the dilating lattice, one could contract the lattice and subsequently load the dipole trap. This will cause fewer 'pancake' potentials to be filled more densely which is useful for experiments.

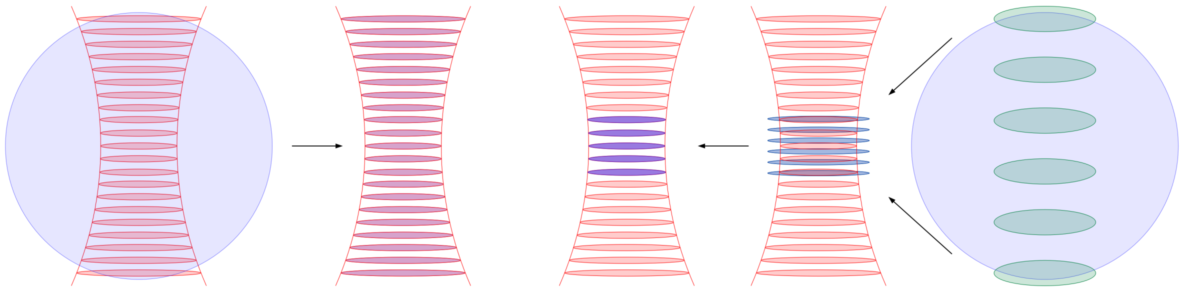

Figure 6.2: A cartoon of both the normal loading of the dipole trap, and the loading via the dilating lattice. The gas cloud in blue can be either loaded directly into the dipole trap, filling a large number of 'pancake' potentials or it can first be loaded into a dilating lattice and contracted to fill a small number of 'pancake' potentials more densely.

Due to the desire to use a wavelength of light smaller than the imaging light's 671nm, one will need to take into consideration the possibility of chromatic aberration in the system. This can be tested by measuring the distance at which the camera must be placed for the image to be focused for different wavelengths of light. As this is a simple test, it will be conducted before any more work is done on the dilating lattice to make sure the current aspheric lens is suitable.

Chapter 7

Conclusions

A vertical imaging system was designed to have a resolution of at least 2μm and properly interface with the current experimental apparatus. The system was subsequently built in stages which allowed for the effect of each component to be characterized. This characterization was done according to the FWHM and intensity of the diffraction pattern caused by a 1μm pinhole. The basic setup was compared to simple theory and was found to have unaccounted for aberrations, although the two converged as the aperture became large. It was shown that placing the aperture after the lens provided a better resolution for the same aperture size when compared with the lens being placed before the aperture. Placing the lens away from the Fourier plane was then shown to enhance some asymmetry that was most likely created by the beam cube.

The criteria for relating the spatial density distribution, from a ToF measurement, with the momentum space distribution of an ultra-cold gas was investigated. This was done in anticipation of using the new imaging system to experimentally test predictions concerning the entanglement entropy of a degenerate fermi gas.

Lastly, the preliminary design for a dilating lattice was discussed as an aid for a pinning lattice and fluorescence imaging, as well as a independent device for manipulating a trapped gas. This was done assuming the same aspheric lens would be used for both the imaging system and the dilating lattice, and hence the method for testing for chromatic aberration was outlined.

Bibliography

[1] Balasubramanian, V., M.B. McDermott and M. Van Raamsdonk, *Phys. Rev. D.* **86** 045014 (2012) [arXiv:1108.3568 [hep-th]].

[2] Hsu, T.L., M.B. McDermott, and M. Van Raamsdonk, arXiv:1210.0054 [hep-th].

[3] Anderson, M.H., J. R. Ensher, M.R. Matthews, C.E. Wieman, and E.A. Cornell, 1995, *Science* **269**, 198 (1995).

[4] Altman, E., E. Demler, and M. D. Lukin, *Phys. Rev. A.* **70** 013603 (2004).

[5] Bakr, W.S., J.I. Gillen, A. Peng, S. Fölling, and M. Greiner, *Nature* **462**, 74 (2009).

[6] Greiner, M., C.A. Regal, J.T. Stewart, and D.S. Jin, *Phys. Rev. Lett.* **94** 110401 (2005).

[7] Gehm, M.E., PhD thesis, Duke University (2003).

[8] Gillen, J.I., PhD thesis, Harvard University (2009).

[9] Nielsen, M.A., and I.L. Chuang, Quantum Computation and Quantum Information *Cambridge University Press, Cambridge* (2000).

[10] Endres, M., M. Cheneau, T. Fukuhara, C. Weitenberg, P. Schauβ, C. Gross, L. Mazza, M.C. Banüls, L. Pollet, I. Bloch and S. Kuhr, *Applied Physics B* **113** 27 (2013).

[11] Sherson, J.F., C. Weitenberg, M. Endres, M. Cheneau, I. Bloch, and S. Kuhr, *Nature* **467** 68 (2010).

[12] Saleh, B.E.A., M.C. Teich, Fundamentals of Photonics *Wiley-Interscience, Hoboken* (2007)

Appendix A

MATLAB Scripts

Here are all the MATLAB scripts used to analyze data and do the theoretical calculations.

A.1 preferences.m

This function is just a basic script to aid main.m. It is a GUI to get the data file's name.

```
function [date data_name]=preferences(save_file,base_dir)
choice=2; save_choice=2;
[date data_name]=img_saves(save_file);
if strcmp(date,'')==0 && strcmp(data_name,'')==0
    choice=menu(sprintf('Would you like to use\nDate: %s\nData File Name: %s',...
        date,data_name),'Yes','No');
end
if choice==2
    d = dir(base_dir);
    str = {d.name};
    [s,v] = listdlg('PromptString','Select a file:','SelectionMode',...
     'single','ListString',str);
    date=str{s};
    d = dir(strcat(base_dir,date,'/'));
    str = {d.name};
    [s,v] = listdlg('PromptString','Select a file:','SelectionMode',...
     'single','ListString',str);
    data_name=str{s};
    save_choice=menu('Save choice?','Yes','No');
end
if save_choice==1
    savefile=fopen(save_file,'w');
    fprintf(savefile,sprintf('#Date Data_Name\n%s %s',...
     date,data_name));
    fclose(savefile);
end
```

A.2 img_saves.m

A helper function for preferences to get the saved preferences.

```
function [date data_name]=img_saves(save_file)
savefile=fopen(save_file,'r');
date='';
data_name='';
if savefile~=-1
    while 1
        tline=fgetl(savefile);
        if ~ischar(tline), break, end
        if ismember('#',tline)
            msg=regexprep(tline,'#','');
        else
            [date data_name]=strtok(tline);
            data_name=strtrim(data_name);
        end
    end
    str_date='There was no previously stored date';
    if strcmp(date,'')==0
        str_date=strcat('The last date was:',' ',date);
    end
    str_data_name='There was no previously stored data file name';
    if strcmp(data_name,'')==0
        str_data_name=strcat('The last data file name was:',' ',data_name);
    end
end
```

A.3 img_info.m

This is another aid script to get the aperture from the filename.

```
function [aperture]=img_info(name)
decimal= strfind(name, '_');
dash=strfind(name,'-');
if isempty(dash)
    dash=decimal(end);
    decimal=decimal(1);
end
```

```
aperture=strcat(name(1:decimal-1),'.',name(decimal+1:dash-1));
```

A.4 get_images.m

This script gets all the images in a data set and sorts them into the actual data and the control, background images.

```
function [images_sorted background]=get_images(data_loc,image_type)
images_w_background = dir(strcat(data_loc,'*.',image_type));
images=cellfun(@background_be_gone,{images_w_background.name},...
'UniformOutput',0);
images=images(~cellfun('isempty',images));
ref=cellfun(@img_info,images,'UniformOutput',0);
[unique_strings, ~, string_map]=unique(ref);
most_common_string=unique_strings(mode(string_map));
frequency=sum(strcmp(ref,most_common_string));
images_sorted=cell(frequency,length(unique(ref)));
ref=unique(ref);
for i=1:length(images)
    aperture=img_info(images{i});
    index=find(strcmp(ref,aperture));
    j=1;
    while isempty(images_sorted{j,index})==0;
        j=j+1;
    end
    images_sorted{j,index}=images{i};
end
background=cellfun(@images_be_gone,{images_w_background.name},'UniformOutput',0);
background=background(~cellfun('isempty',background));
```

A.5 images_be_gone.m

A simple helper function for get_images.m to remove all the data images from an array of images to leave only the background images.

```
function name_out=images_be_gone(name_in)
if strfind(name_in,'background')
    name_out=name_in;
else
```

```
    name_out=[];
end
```

A.6 background_be_gone.m

Like images_be_gone.m, this gets rid of the background images so that only the data images are left.

```
function name_out=background_be_gone(name_in)
if strfind(name_in,'background')
    name_out=[];
else
    name_out=name_in;
end
```

A.7 img_load.m

This loads all of the images with get_images.m, subtracts the average of the background images, and then averages them.

```
function all_images=img_load(data_dir,date, data_file_name,image_type)
data_loc=strcat(data_dir,date,'/',data_file_name,'/Data/');
background_image=0;
[images background]=get_images(data_loc,image_type);
[number_per_trial number_of_apertures]=size(images);
all_images=cell(number_of_apertures,number_per_trial+1);

for i=1:length(background)
    background_image_string=strcat(data_loc,background{i});
    if strcmp(image_type,'png')
        background_image_temp=double(imread(background_image_string));
    else
        background_image_temp=double(fitsread(background_image_string));
    end
    background_image=background_image+background_image_temp;
end
background_image=uint16(background_image/length(background));

for i=1:number_of_apertures
```

```
    for j=1:number_per_trial
        if isempty(images{j,i})
            break
        end
        all_images{i,1}=img_info(images{j,i});
        image_string=strcat(data_loc,images{j,i});
        if strcmp(image_type,'png')
            image_raw_temp=imread(image_string)-background_image;
        else
            image_raw_temp=uint16(fitsread(image_string))-background_image;
        end
        all_images{i,j+1}=image_raw_temp;
    end
end
```

A.8 img_average.m

This takes all the images, after the background has been subtracted, and filters out the images without a high enough intensity when compared to the highest intensity image. Then it averages all the images based off of their aperture so that the output gives one image per aperture size.

```
function average_images=img_average(all_images,threshold)
[number_of_apertures number_of_trials]=size(all_images);
average_images=[all_images(1:end,1) num2cell(zeros(number_of_apertures,1))];
for i=1:number_of_apertures
    temp1=all_images(i,2:end);
    temp=temp1(~cellfun('isempty',temp1));
    filtered_images=image_filter(temp,threshold);
    for j=1:length(filtered_images)
        average_images{i,2}=average_images{i,2}+double(filtered_images{j});
    end
    average_images{i,2}=average_images{i,2}/length(filtered_images);
end
```

A.9 image_filter.m

This is the helper function that actually filters the images based off of how intense they are relative to the most intense image of that aperture size.

```
function filtered_images=image_filter(images,threshold)
```

```
[average maximum]=cellfun(@filter_supplemental,images,'UniformOutput',0);
filtered_images=images(cell2mat(maximum)>=threshold*max(cell2mat(maximum)));
```

A.10 filter_supplemental.m

This is another helper function for cellfun(.).

```
function [average maximum]=filter_supplemental(image)
average=mean(image(:));
maximum=max(image(:));
```

A.11 max_loc.m

Given an image and some threshold fraction, this script finds, what should be, the maximum. It uses a weighted mean to try to find the peak. This way it isn't as susceptible to random fluctuations in intensity.

```
function [maxloc_x maxloc_y]=max_loc(image,threshold_frac)
threshold_frac=0.9;
[width height]=size(image);
lib=reshape(1:(width*height),width,height);
threshold=threshold_frac*max(image(:));
loc_temp=lib(image>=threshold);

[maxloc_y maxloc_x] = ind2sub(size(image), loc_temp);
maxloc_y=round(wmean(maxloc_y,image(loc_temp).^3));
maxloc_x=round(wmean(maxloc_x,image(loc_temp).^3));

if isnan(maxloc_y)
    maxloc_y=width/2;
end
if isnan(maxloc_x)
    maxloc_x=width/2;
end
```

A.12 image_fit.m

This function looks at two cross sections of the image, one in the vertical direction the the peak and one in the horizontal direction. It then fits the data along these directions. An example of what this would look like is given in Figure A.1.

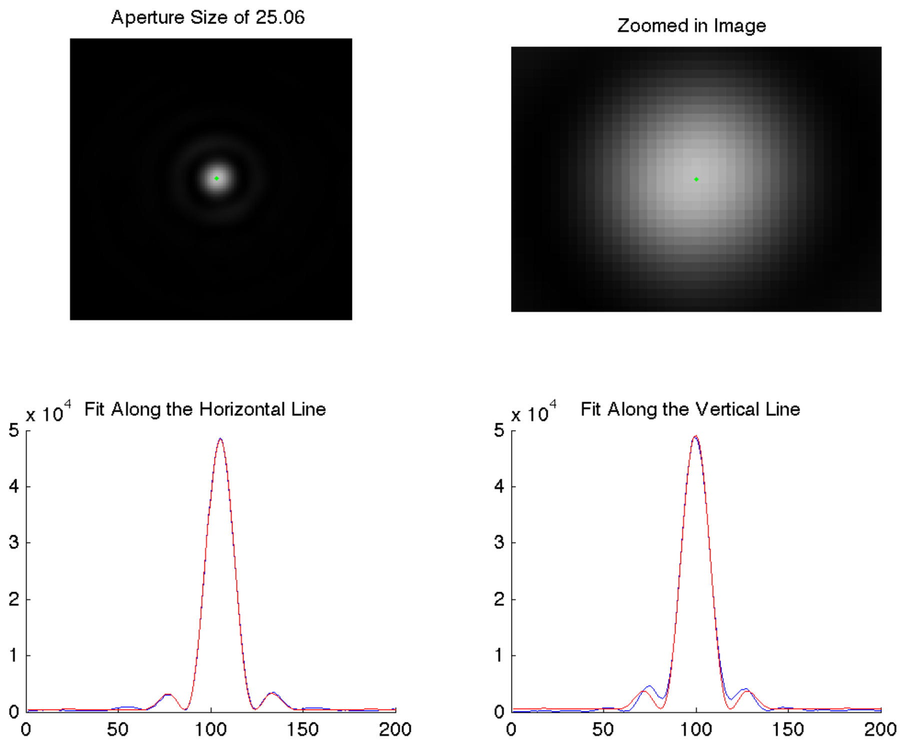

Figure A.1: An example of how the data is fit. The green point in the top two images is what max_loc.m has determined to be the maximum. The two lines in the top to images are the vertical and horizontal data sets that it fits. Those data sets, and their fits are plotted in the bottom to subfigures.This image is from Stage 3 and notice the data along the vertical has some spherical aberrations that are indicated by the elevated minima.

```
function output=image_fit(image,maxloc_x,maxloc_y)
height_0=1000.0;
width_0=10.0;

I_hor=image(maxloc_y,:);
I_vert=image(:,maxloc_x)';

f=@(p,x) p(1)*abs((1/(1-p(2)^2)^2)*((2./((x-p(3))/p(4))).^2). ...
*(besselj(1,(x-p(3))/p(4))-p(2)*besselj(1,p(2)*(x-p(3))/p(4))).^2)+p(5);

x_hor=1:length(I_hor);
p0_hor=[max(I_hor) 0 maxloc_x width_0 min(I_hor)];
fitf_hor = @(p) sum(((I_hor-f(p,x_hor)).^2));
```

```
p_hor=fminsearch(fitf_hor,p0_hor);

x_vert=1:length(I_vert);
p0_vert=[max(I_vert) 0 maxloc_y width_0 min(I_vert)];
fitf_vert = @(p) sum(((I_vert-f(p,x_vert)).^2));
p_vert=fminsearch(fitf_vert,p0_vert);

output=[{I_hor},{I_vert},{p_hor},{p_vert}];
```

A.13 theory.m

This is the function that is responsible for the simple model in Section 3.3.

```
function [D x output FWHM]=theory(w,l,res)
D=linspace(1,50,30);
f=40*10^-3;
x=linspace(-10^-5,10^-5,res);

g=@(x) p(1)*(besselj(1,p(2)*abs(x-p(3)))./abs(x-p(3))).^2 -p(4);

x=x(x~=0);
y=linspace(-w/2.,w/2.,res);
y2=repmat(y,length(x),1);
x2=repmat(x',1,res);
temp=x2+y2;
[a b]=size(temp);
output=zeros(length(D),a);
p=cell(length(D),1);

for j=1:length(D)
    p{j}=[(D(j)/4)^2,2*pi*(10^-3)*D(j)/(l*f),0,0];
    airy=airy_func(p{j},temp);
    for i=1:a
       output(j,i)=trapz(temp(i,:),airy(i,:));
    end
end

FWHM=zeros(length(D),1);
```

```
for i=1:length(D)
    FWHM(i)=fwhm(x,output(i,:));
end

[s, mess, messid] = mkdir('../Data/Theory', sprintf('%g_%g',w*10^6,l*10^9));
x_file_name=sprintf('/Users/user/Documents/School/Physics_Honours_Thesis/Data/
Theory/%g_%g/x_file.txt',w*10^6,l*10^9);
D_file_name=sprintf('/Users/user/Documents/School/Physics_Honours_Thesis/Data/
Theory/%g_%g/D_file.txt',w*10^6,l*10^9);
output_file_name=sprintf('/Users/user/Documents/School/Physics_Honours_Thesis/Data/
Theory/%g_%g/output_file.txt',w*10^6,l*10^9);
FWHM_file_name=sprintf('/Users/user/Documents/School/Physics_Honours_Thesis/Data/
Theory/%g_%g/FWHM_file.txt',w*10^6,l*10^9);

csvwrite(D_file_name,D);
csvwrite(FWHM_file_name,FWHM);
csvwrite(x_file_name,x);
csvwrite(output_file_name,output);
```

A.14 airy_conv.m

This is a helper function to take the convolution of an Airy function and a rect function.

```
function [value]=airy_conv(x_0,p,w)
f=@(p,x) p(1)*(besselj(1,p(2)*abs(x-p(3)))./(p(2)*abs(x-p(3)))).^2 -p(4);
x=linspace(x_0-(w/2.),x_0+(w/2.),10000);
x=x(x~=p(3));
airy=f(p,x);
value=trapz(x,airy);
```

A.15 magnification_main.m

This is the main script for determining the magnification of a data set. It calls a variety of helper functions to load the correct images and then it fits them and determines the relationship between pinhole and image translations. This is done by linearly fitting the data as is depicted in Figure 4.1.

```
clc
clf
```

```
clear all
close all

f=@(p,x) p(1)*abs((1/(1-p(2)^2)^2)*((2./((x-p(3))/p(4))).^2). ...
*(besselj(1,(x-p(3))/p(4))-p(2)*besselj(1,p(2)*(x-p(3))/p(4))).^2)+p(5);
Image_Distances_x=[];
Image_Distances_y=[];
save_file=['/Users/user/Documents/School/Physics_Honours_Thesis/Scripts/'...
'Script_Files/Magnification_Fit_Preference_Saves.txt'];
data_dir='/Users/user/Documents/School/Physics_Honours_Thesis/Data/';

[date data_file_name]=preferences(save_file,data_dir);
plots_loc=strcat(data_dir,date,'/',data_file_name,'/Plots/');

image_types={'png','fit'};
image_type=image_types{menu('Image type?',image_types)};
all_images=img_load(data_dir,date,data_file_name,image_type);

average_images=img_average(all_images,0.95);
temp=size(average_images);
number_of_distances=temp(1);

maxloc=[{'Distance', 'Max_X_Coordinate','Max_Y_Coordinate'};
average_images(1:end,1),num2cell(zeros(number_of_distances,2))];

for i=1:number_of_distances
     [maxloc_x maxloc_y]=max_loc(double(average_images{i,2}),0.9);
    maxloc{i+1,2}=maxloc_x;
    maxloc{i+1,3}=maxloc_y;
end

I_hor=[average_images(1:end,1) num2cell(zeros(number_of_distances,1))];
I_vert=[average_images(1:end,1) num2cell(zeros(number_of_distances,1))];
p_hor=[average_images(1:end,1) num2cell(zeros(number_of_distances,1))];
p_vert=[average_images(1:end,1) num2cell(zeros(number_of_distances,1))];

for i=1:number_of_distances
    temp=image_fit(double(average_images{i,2}),maxloc{i+1,2},maxloc{i+1,3});
```

```
    I_hor{i,2}=temp{1};
    I_vert{i,2}=temp{2};
    p_hor{i,2}=temp{3};
    p_vert{i,2}=temp{4};
end

for i=1:number_of_distances
    h=figure();
    subplot(2,2,1)
    imshow(uint16(average_images{i,2}))
    hold on
    title(sprintf('Distance of %0.5g',str2double(average_images{i,1})));
    plot(maxloc{i+1,2},maxloc{i+1,3},'g.')
    hold off

    subplot(2,2,2)
    imshow(uint16(average_images{i,2}))
    hold on
    title('Zoomed in Image');
    plot(maxloc{i+1,2},maxloc{i+1,3},'g.')
    axis([maxloc{i+1,2}-21,maxloc{i+1,2}+21,maxloc{i+1,3}-15,maxloc{i+1,3}+15])
    hold off

    x_hor=1:length(I_hor{i,2});
    x_vert=1:length(I_vert{i,2});

    subplot(2,2,3)
    hold on
    plot(x_hor,I_hor{i,2})
    plot(x_hor,f(p_hor{i,2:end},x_hor),'r')
    title('Fit Along the Horizontal Line')
    hold off

    subplot(2,2,4)
    hold on
    plot(x_vert,I_vert{i,2})
    plot(x_vert,f(p_vert{i,2:end},x_vert),'r')
    plot(x_vert,f([max(I_vert{i,2}) 0 maxloc{i+1,3} ...
```

```
     15 min(I_vert{i,2})],x_vert),'r')
    title('Fit Along the Vertical Line')
    hold off

    Intensity_hor{i,2}=p_hor{i,2}(1)+p_hor{i,2}(5);
    Intensity_vert{i,2}=p_vert{i,2}(1)+p_vert{i,2}(5);

    temp_hor=abs(0.5*p_hor{i,2}(1)+p_hor{i,2}(5)-f(p_hor{i,2},x_hor));
    FWHM_hor{i,2}=2*abs(p_hor{i,2}(3)-x_hor(temp_hor==min(temp_hor)));

    temp_vert=abs(0.5*p_vert{i,2}(1)+p_vert{i,2}(5)-f(p_vert{i,2},x_vert));
    FWHM_vert{i,2}=2*abs(p_vert{i,2}(3)-x_vert(temp_vert==min(temp_vert)));

    Image_Distances_x=[p_hor{i,2}(3) Image_Distances_x];
    Image_Distances_y=[p_vert{i,2}(3) Image_Distances_y];
end
Distances=cell2mat(cellfun(@str2num,maxloc(2:end,1),'UniformOutput',0));

%tick_convert=1.0/50; %Conversions for measurements on different translations stages.
tick_convert=0.0011;
pixel_convert=6.8*0.001; %i.e. 1 pixel is 6.8*0.001 mm
d=tick_convert*Distances';
x=pixel_convert*Image_Distances_x;
y=pixel_convert*Image_Distances_y;

linear_f=@(p,x) p(1)*x+p(2);
linear_fitf_x=@(p) sum((x-linear_f(p,d)).^2);
linear_fitf_y=@(p) sum((y-linear_f(p,d)).^2);
p0_x=[mean(x)/mean(d),100];
p0_y=[mean(y)/mean(d),100];
p_x=fminsearch(linear_fitf_x,p0_x);
p_y=fminsearch(linear_fitf_y,p0_y);
t=linspace(min(d),max(d),1000);
h=figure();
hold on
plot(d,x,'r+')
plot(t,linear_f(p_x,t))
hold off
```

```
h=figure();
hold on
plot(d,y,'r+')
plot(t,linear_f(p_y,t))
hold off
```

A.16 main.m

This is the main script for determining the FWHM and intensity trends in each data set. It saves this data so that it can be plotted or analyzed further at some later point.

```
clc
clf
clear all
close all

f=@(p,x) p(1)*abs((1/(1-p(2)^2)^2)*((2./((x-p(3))/p(4))).^2). ...
*(besselj(1,(x-p(3))/p(4))-p(2)*besselj(1,p(2)*(x-p(3))/p(4))).^2)+p(5);

save_file=['/Users/user/Documents/School/Physics_Honours_Thesis/Scripts/',...
'Script_Files/Diffraction_Fit_Preference_Saves.txt'];
data_dir='/Users/user/Documents/School/Physics_Honours_Thesis/Data/';

[date data_file_name]=preferences(save_file,data_dir);
plots_loc=strcat(data_dir,date,'/',data_file_name,'/Plots/');

image_types={'png','fit'};
image_type=image_types{menu('Image type?',image_types)};
all_images=img_load(data_dir,date,data_file_name,image_type);

average_images=img_average(all_images,0.95);
temp=size(average_images);
number_of_apertures=temp(1);

maxloc=[{'Aperture', 'Max_X_Coordinate','Max_Y_Coordinate'};
average_images(1:end,1),num2cell(zeros(number_of_apertures,2))];

for i=1:number_of_apertures
```

```
    [maxloc_x maxloc_y]=max_loc(double(average_images{i,2}),0.9);
    maxloc{i+1,2}=maxloc_x;
    maxloc{i+1,3}=maxloc_y;
end

I_hor=[average_images(1:end,1) num2cell(zeros(number_of_apertures,1))];
I_vert=[average_images(1:end,1) num2cell(zeros(number_of_apertures,1))];
p_hor=[average_images(1:end,1) num2cell(zeros(number_of_apertures,1))];
p_vert=[average_images(1:end,1) num2cell(zeros(number_of_apertures,1))];

for i=1:number_of_apertures
    temp=image_fit(double(average_images{i,2}),maxloc{i+1,2},maxloc{i+1,3});
    I_hor{i,2}=temp{1};
    I_vert{i,2}=temp{2};
    p_hor{i,2}=temp{3};
    p_vert{i,2}=temp{4};
end

Intensity_hor=[average_images(1:end,1) num2cell(zeros(number_of_apertures,1))];
Intensity_vert=[average_images(1:end,1) num2cell(zeros(number_of_apertures,1))];
FWHM_hor=[average_images(1:end,1) num2cell(zeros(number_of_apertures,1))];
FWHM_vert=[average_images(1:end,1) num2cell(zeros(number_of_apertures,1))];

for i=1:number_of_apertures
    h=figure();
    subplot(2,2,1)
    imshow(uint16(average_images{i,2}))
    hold on
    title(sprintf('Aperture Size of %0.5g',str2double(average_images{i,1})));
    plot(maxloc{i+1,2},maxloc{i+1,3},'g.')
    hold off

    subplot(2,2,2)
    imshow(uint16(average_images{i,2}))
    hold on
    title('Zoomed in Image');
    plot(maxloc{i+1,2},maxloc{i+1,3},'g.')
    axis([maxloc{i+1,2}-21,maxloc{i+1,2}+21,maxloc{i+1,3}-15,maxloc{i+1,3}+15])
```

```
    hold off

    x_hor=1:length(I_hor{i,2});
    x_vert=1:length(I_vert{i,2});

    subplot(2,2,3)
    hold on
    plot(x_hor,I_hor{i,2})
    plot(x_hor,f(p_hor{i,2:end},x_hor),'r')
    title('Fit Along the Horizontal Line')
    hold off

    subplot(2,2,4)
    hold on
    plot(x_vert,I_vert{i,2})
    plot(x_vert,f(p_vert{i,2:end},x_vert),'r')
    title('Fit Along the Vertical Line')
    hold off

    Intensity_hor{i,2}=p_hor{i,2}(1)+p_hor{i,2}(5);
    Intensity_vert{i,2}=p_vert{i,2}(1)+p_vert{i,2}(5);

    temp_hor=abs(0.5*p_hor{i,2}(1)+p_hor{i,2}(5)-f(p_hor{i,2},x_hor));
    FWHM_hor{i,2}=2*abs(p_hor{i,2}(3)-x_hor(temp_hor==min(temp_hor)));

    temp_vert=abs(0.5*p_vert{i,2}(1)+p_vert{i,2}(5)-f(p_vert{i,2},x_vert));
    FWHM_vert{i,2}=2*abs(p_vert{i,2}(3)-x_vert(temp_vert==min(temp_vert)));

    saveas(h,strcat(plots_loc,average_images{i,1},'_figure','.png'));
end


Apertures=cell2mat(cellfun(@str2num,Intensity_hor(:,1),'UniformOutput',0));
Intensities_hor=cell2mat(Intensity_hor(:,2));
Intensities_vert=cell2mat(Intensity_vert(:,2));
FWHM_hor_temp=cell2mat(FWHM_hor(:,2));
FWHM_vert_temp=cell2mat(FWHM_vert(:,2));
[Apertures_sorted, SortIndex] = sort(Apertures);
```

```
Intensities_hor_sorted=Intensities_hor(SortIndex);
Intensities_vert_sorted=Intensities_vert(SortIndex);
FWHM_hor_sorted=FWHM_hor_temp(SortIndex);
FWHM_vert_sorted=FWHM_vert_temp(SortIndex);
figure()
semilogy(Apertures_sorted,Intensities_hor_sorted,'.')
hold on
semilogy(Apertures_sorted,Intensities_hor_sorted)
semilogy(Apertures_sorted,Intensities_vert_sorted,'.r')
semilogy(Apertures_sorted,Intensities_vert_sorted,'r')
hold off

figure()
plot(Apertures_sorted,FWHM_hor_sorted,'.')
hold on
plot(Apertures_sorted,FWHM_hor_sorted)
plot(Apertures_sorted,FWHM_vert_sorted,'.r')
plot(Apertures_sorted,FWHM_vert_sorted,'r')
hold off

data_loc=strcat(data_dir,date,'/',data_file_name,'/Data/');

Intensity_file=fopen(strcat(data_loc,'Intensity_file.txt'),'w');
Intensity=[Apertures_sorted';Intensities_hor_sorted';Intensities_vert_sorted']
fprintf(Intensity_file,'%12s\t%12s\t%12s\n','&aperture','column','row');
fprintf(Intensity_file,'%12.8f\t%12.8f\t%12.8f\n',Intensity);
fclose(Intensity_file);


FWHM_file=fopen(strcat(data_loc,'FWHM_file.txt'),'w');
FWHM=[Apertures_sorted';FWHM_hor_sorted';FWHM_vert_sorted']
fprintf(FWHM_file,'%12s\t%12s\t%12s\n','&aperture','column','row');
fprintf(FWHM_file,'%12.8f\t%12.8f\t%12.8f\n',FWHM);
fclose(FWHM_file);
```

A.17 fwhm.m

This is a function to determine the FWHM of a waveform.

```
function width = fwhm(x,y)
% function width = fwhm(x,y)
%
% Full-Width at Half-Maximum (FWHM) of the waveform y(x)
% and its polarity.
% The FWHM result in 'width' will be in units of 'x'
%
%
% Rev 1.2, April 2006 (Patrick Egan)



y = y / max(y);
N = length(y);
lev50 = 0.5;
if y(1) < lev50                  % find index of center (max or min) of pulse
    [garbage,centerindex]=max(y);
    Pol = +1;
    %disp('Pulse Polarity = Positive')
else
    [garbage,centerindex]=min(y);
    Pol = -1;
    %disp('Pulse Polarity = Negative')
end
i = 2;
while sign(y(i)-lev50) == sign(y(i-1)-lev50)
    i = i+1;
end                                   %first crossing is between v(i-1) & v(i)
interp = (lev50-y(i-1)) / (y(i)-y(i-1));
tlead = x(i-1) + interp*(x(i)-x(i-1));
i = centerindex+1;                    %start search for next crossing at center
while ((sign(y(i)-lev50) == sign(y(i-1)-lev50)) & (i <= N-1))
    i = i+1;
end
if i ~= N
```

```
    Ptype = 1;
    %disp('Pulse is Impulse or Rectangular with 2 edges')
    interp = (lev50-y(i-1)) / (y(i)-y(i-1));
    ttrail = x(i-1) + interp*(x(i)-x(i-1));
    width = ttrail - tlead;
else
    Ptype = 2;
    %disp('Step-Like Pulse, no second edge')
    ttrail = NaN;
    width = NaN;
end
```

A.18 wmean.m

This is a function to find the weighted mean of some data.

```
function wm = wmean(X,W,dim)
% wmean: compute a weighted mean along a given dimension
% Usage: wm = wmean(X,W,dim)
%
% Arguments: (input)
% X - vector or array of any dimension
%
% W - (OPTIONAL) vector of weights, must be the same length
% as the size of X in the specified dimension. If W is
% not supplied or is left empty, then the built-in mean
% is called.
%
% At least one weight must be a positive number, all
% must be non-negative.
%
% dim - (OPTIONAL) positive integer scalar - denotes the
% dimension to compute the weighted mean over.
%
% If dim is not specified, then it will be the first
% dimension that matches the length of W.
%
% Arguments: (output)
```

```
% wm - weighted mean array (or vector). wm will be
% the same shape/size as X, except in the specified
% dimension.
%
% Example:
% X = rand(3,5);
% wmean(X,[0 1 3.5],1)
% ans =
% 0.19754 0.53772 0.49303 0.61549 0.13113
%
% See also: mean, median, mode, var, std
%
% Author: John D'Errico
% e-mail: woodchips@rochester.rr.com
% Release: 1.0
% Release date: 7/7/08

if (nargin==1) || (isempty(W) && (nargin<3))
  % no weights, no dim
  wm = mean(X);
  return
elseif isempty(W)
  % no weights, dim provided
  wm = mean(X,dim);
  return
end

% weights were provided, and were not empty
if ~isvector(W)
  error('W must be a vector.')
end
W = W(:);
if any(W<0)
  error('All weights must be non-negative')
elseif all(W==0)
  error('At least one must be positive')
end
nw = length(W);
```

```
nx = size(X);

% Normalize the weight vector to unit 1-norm
W = W/norm(W,1);

% we need to find dim?
if (nargin<3) || isempty(dim)
  dim = find(nx==nw,1,'first');
  if isempty(dim)
    dim = 1;
  end
elseif (dim<=0) || ~isscalar(dim) || dim~=round(dim)
  error('dim must be a positive integer scalar')
end
if nx(dim) ~= nw
  error('Weight vector is incompatible with size of X')
end

% compute the weighted mean - use bsxfun, then
% just sum down the specified dimension.
Wshape = ones(1,length(nx));
Wshape(dim) = nw;
wm = sum(bsxfun(@times,X,reshape(W,Wshape)),dim);
```